Summer 2024

Low Finesse Extrinsic Fabry-Perot Interferometer (Efpi) Demodulation for High Temperature Gap Measurements

Abhishek Prakash Hungund
Missouri University of Science and Technology

Department:

Recommended Citation

Prakash Hungund, Abhishek, "Low Finesse Extrinsic Fabry-Perot Interferometer (Efpi) Demodulation for High Temperature Gap Measurements" (2024). *Masters Theses*. 8192.
https://scholarsmine.mst.edu/masters_theses/8192

LOW FINESSE EXTRINSIC FABRY-PEROT INTERFEROMETER (EFPI) DEMODULATION FOR HIGH TEMPERATURE GAP MEASUREMENTS

by

ABHISHEK PRAKASH HUNGUND

A THESIS

Presented to the Graduate Faculty of the

MISSOURI UNIVERSITY OF SCIENCE AND TECHNOLOGY

In Partial Fulfillment of the Requirements for the Degree

MASTER OF SCIENCE

in

COMPUTER ENGINEERING

2023

Approved by:

Jie Huang, Advisor
Rex E. Gerald II
Mina Esmaeelpour
Steve Watkins

PUBLICATION THESIS OPTION

This thesis consists of the following article, formatted in the style used by the Missouri University of Science and Technology:

Paper I, found on pages 20–58, has been submitted to *IEEE Transactions on Instrumentation and Measurement*.

ABSTRACT

In continuous casting steel industries, mold flux is added to provide thermal and chemical insulation for molten steel. The mold flux absorbs detrimental inclusions from the steel and promotes uniform heat distribution to prevent sticking. To promote flux infiltration, mold oscillation is used, but this creates oscillation marks that reduce local shell growth and increase temperatures. Wide (2-3 mm) and deep (0.5-0.9 mm) oscillation marks with areas of 1.1-2.5 mm^2 are observed, affecting the steel quality, which results in a loss of 6% per billet to the industry. To address this challenge, we propose an extrinsic Fabry-Perot interferometer (EFPI) sensor for high-temperature gap measurements. The proposed EFPI sensor has a wide measurement range of 10 µm to 1000 µm with a measurement uncertainty of 5 to 8 nm, and for larger gaps in the range of 1000 µm to 3.5 mm, the measurement uncertainty is 0.1 to 0.3 µm.

The EFPI sensors measure the gap during shrinkage due to rapid cooling of the flux material in real-time, providing a reliable and accurate measurement method for high-temperature gap sensing in a harsh environment. A smaller air gap between mold and solidified mold flux is favorable for strand lubrication and the thickness of mold flux film are crucial for production of higher-quality steel. A lower melting temperature of mold flux leads to greater liquid slag thicknesses and smaller maximum air gap thicknesses. A shortage of flux feeding into the gap can lead to air gaps, non-uniform heat flow, thinning of the shell, and longitudinal surface cracks. Thus, measuring the air gap and thickness of the mold flux aids in optimizing the melting temperature, flux feeding and mold oscillation frequency which can improve overall casting process.

ACKNOWLEDGMENTS

I wanted to take a moment to express my deepest appreciation and gratitude to everyone who has played a part in my academic journey towards achieving a Master's degree in Computer Engineering. Your unwavering support, guidance, and generosity have been instrumental in helping me reach this significant milestone. Firstly, I would like to extend my heartfelt thanks to Dr. Jie Huang, whose dedication and mentorship have been invaluable throughout the past two years. Dr. Huang's courses have provided me with a solid foundation of knowledge that will undoubtedly benefit me in my future endeavors. His passion for learning and exploration has inspired me to pursue my interests in the field of Microwave Photonics in my future. I would also like to express my gratitude to Dr. Rex E. Gerald II for his constant guidance and mentorship throughout my studies. His infectious enthusiasm and persistence have led to success in many projects during my research. I am truly grateful for his unwavering support. In addition, I would like to thank Dr. Mina Esmaeelpour and Dr. Steve E. Watkins for serving on my committee and for their invaluable insights and expertise. Additionally, I would like to thank Dr. Ronald O'Malley for his unwavering support throughout my research. Special thanks go to Dr. Bohong Zhang for supporting me in pursuing other research avenues apart from my thesis and helping me publish my work. I am also incredibly grateful for the support of all my colleagues in the Lightwave Technology Lab. Their encouragement and shared passion for research have made this journey more rewarding. Lastly, I want to express my heartfelt gratitude to my parents, siblings, and friends for their love and unwavering support. Their encouragement has been instrumental in all that I have accomplished in my life thus far.

TABLE OF CONTENTS

Page

SECTION

PAPER

SECTION

LIST OF ILLUSTRATIONS

SECTION Page

PAPER I Page

LIST OF TABLES

NOMENCLATURE

Symbol	Description
SMF	Single-Mode Fiber
EFPI	Extrinsic Fabry-Perot Interferometer
CCMF	Continuous Caster Mold Flux
API	Application Programming Interface
DAQ	Data Acquisition

1. INTRODUCTION

1.1. ISSUES DURING CONTINUOUS CASTING OF STEEL BILLETS

When molten steel solidifies at the mold wall in the continuous casting process, several problems can occur. One of the major issues is the formation of cracks in the cast metal due to uneven cooling and thickening of the steel shell [1]. Another common problem is porosity in the metal due to the release of gas as the metal solidifies [2]. In addition, impermeability in the mold can lead to gas bubbles being trapped inside the metal, resulting in pinholes and other casting defects [3].

1.2. MOLD FLUX AND ITS FEATURES

Mold flux is a material used in the continuous casting of metals, particularly steel. It is a mixture of several compounds, including oxides, fluoride, and alkalis, that is applied to the surface of the casting mold to prevent the molten metal from adhering to the mold and to facilitate the smooth flow of the metal through the mold [4]. Mold flux is applied to the surface of the mold to prevent the molten metal from sticking to the mold and to reduce the formation of surface defects such as surface cracks, surface bubbles, and slag inclusions [5]. It also helps to control the rate of solidification and to minimize the formation of unwanted phases in the final product [6]. The shrinkage of mold flux refers to the reduction in volume or size that occurs when the mold flux material solidifies during the continuous casting process of metals. It can affect the quality of steel in several ways: (a) surface quality – if mold flux shrinks too much, it can crack and cause surface defects in steel, (b) Adhesion – lack of controlled solidification of mold flux leads to uneven coverage of mold surface, and (c) cooling rate – lack controlled cool down results in undesired microstructures on steel’s surface. Therefore, controlling the shrinkage of mold flux is critical for ensuring the quality, efficiency, and cost-effectiveness of the continuous casting process of metals. Thus, measuring the mold flux air gap and thickness allows for identifying the surface defects and provides insight into the material behavior such as crystallization and solidification during its rapid cool down or quenching.

1.3. EXISTING STEEL SURFACE DEFECT DETECTION METHODS

Vision-based defect detection algorithms are widely used to detect surface defects on steel billets. These methods rely on simple pixel-domain vision-based operations, deep learning algorithms, and morphological Top-Hat transform method for detecting corner cracks, sponge cracks, and other surface defects on steel billets [7]. However, these methods require gathering much data and increase time to production. The other types include ultrasonic [8], eddy current [9], X-ray [10], magnetic particle and liquid penetrant testing [11]. Optical surface defect detection systems have several advantages over the non-destructive (NDT) methods in terms of speed, accuracy, non-contact or non-invasive and cost effective.

1.4. ADVANTAGES OF FIBER OPTIC SENSING TECHNOLOGY

Fiber optic sensors are devices that use optical fibers to measure physical or chemical parameters such as temperature [12], pressure [13], strain [14], or the presence of specific chemicals [15]. These sensors operate by detecting changes in the light transmitted through the fiber optic cable due to variations in the parameter being measured. Fiber optic sensors are made up of a light source, an optical fiber that transmits the light, a sensing element that interacts with the parameter being measured, and a photodetector that measures changes in the light transmitted through the fiber. One of the main advantages of fiber optic sensors is their immunity to electromagnetic interference, which makes them ideal for use in harsh environments where traditional sensors may be susceptible to interference or damage. Fiber optic sensors are also highly sensitive, accurate, and can be used over long distances without signal degradation. As a result, fiber optic sensors are widely used in various applications, including aerospace [16], civil engineering [17], oil and gas [18], biomedical [19], environmental monitoring [20] and material studies [21].

1.5. EFPIS AND THEIR APPLICATION IN SENSING TECHNOLOGY

Extrinsic Fabry-Perot interferometers (EFPIs) are fiber optic sensors that use the principles of interferometry to measure physical parameters such as temperature, pressure, or strain [22,23]. They consist of a Fabry-Perot cavity that is formed between two partially reflective surfaces, usually created by cleaving or polishing the ends of two optical fibers or by using a thin film coating. When light is introduced into the cavity, it is partially reflected by the two surfaces and the reflected waves interfere with each other, producing an interference pattern. This interference pattern changes when the length of the cavity changes, either due to a change in the physical parameter being measured or due to external perturbations such as vibration or movement [24]. EFPIs are called "extrinsic" because the Fabry-Perot cavity is not formed within the fiber itself, but rather between two external surfaces. This makes them easier to manufacture and more robust than intrinsic Fabry-Perot interferometers (IFPIs), which require the creation of a cavity within the fiber [25].

EFPIs can be used to measure a wide range of physical parameters such as temperature, pressure, strain, and vibration, and can be designed for use in a variety of applications such as aerospace [26], civil engineering [27], and biomedical sensing [28]. They are known for their high sensitivity, fast response time, and immunity to electromagnetic interference, making them ideal for use in harsh environments [29]. Owing to these features and advantages of the fiber optic EFPI sensors, it is used as point gap sensor to measure air gap and thickness of the mold flux. The air gap and thickness manifest as a consequence of the molten mold flux shrinkage during its crystallization and solidification phenomena.

1.6. EFPI DEMODULATION SYSTEMS

There are several methods for demodulating EFPI interferogram in fiber optic sensors. Some commonly used methods are intensity, phase, wavelength, and polarization demodulation. These demodulation methods can be used individually or in combination to extract different types of information from EFPI sensors, depending on the specific application requirements. Each method has its advantages and limitations, and the choice of demodulation method depends on factors such as the required measurement accuracy, sensitivity, and signal-to-noise ratio, as well as the environmental conditions in which the sensor will be used. Wavelength demodulation is a method for extracting information from the signal or interferogram generated by an EFPI fiber optic sensor. In this method, the EFPI interferogram is converted into a wavelength signal by measuring the change in the wavelength of the light that is reflected or transmitted through the EFPI cavity. Throughout this research, broadband swept laser is used as source to obtain the EFPI interferogram.

Wavelength demodulation is carried out to extract the cavity length information in real-time from the EFPI interferogram.

1.7. OBJECTIVES OF RESEARCH

The following objectives were achieved as part of this thesis work and the have been validated by the paper and further discussion:

1. Design of an EFPI sensor and 3-part stainless-steel mold.
2. Measurement principle of the EFPI interferogram.
3. Real-time low finesse EFPI demodulation algorithm.
4. Demonstration of real-time measurement of air gap and thickness of molten flux during crystallization and solidification

The results of this research are presented in the section of the submitted journal paper in this thesis. It can be summarized as follows:

Primarily, the current understanding of the mathematical basis for air gap and thickness estimation from EFPI interferogram is described, focusing on the physical cavity length change. Additionally, mathematical models to obtain information regarding mold flux transparency is explained.

Further, in Paper I, a 3-part mold is designed with step profile to quench the molten flux. Three EFPI sensors are installed in center of each step of the step profile in the mold to measure air gap and thickness of the molten flux during quenching in real-time. Corresponding EFPI interferograms are presented and analyzed along with the air gap and thickness measurements.

Lastly, a new modified experimental setup is proposed for controlled quenching of the mold flux. This enables the mold flux to undergo crystallization phase for longer duration providing more information. Suggestions for future work are provided for continued development of this method in the field of material science and fiber-optic sensing.

2. BACKGROUND

2.1. OVERVIEW

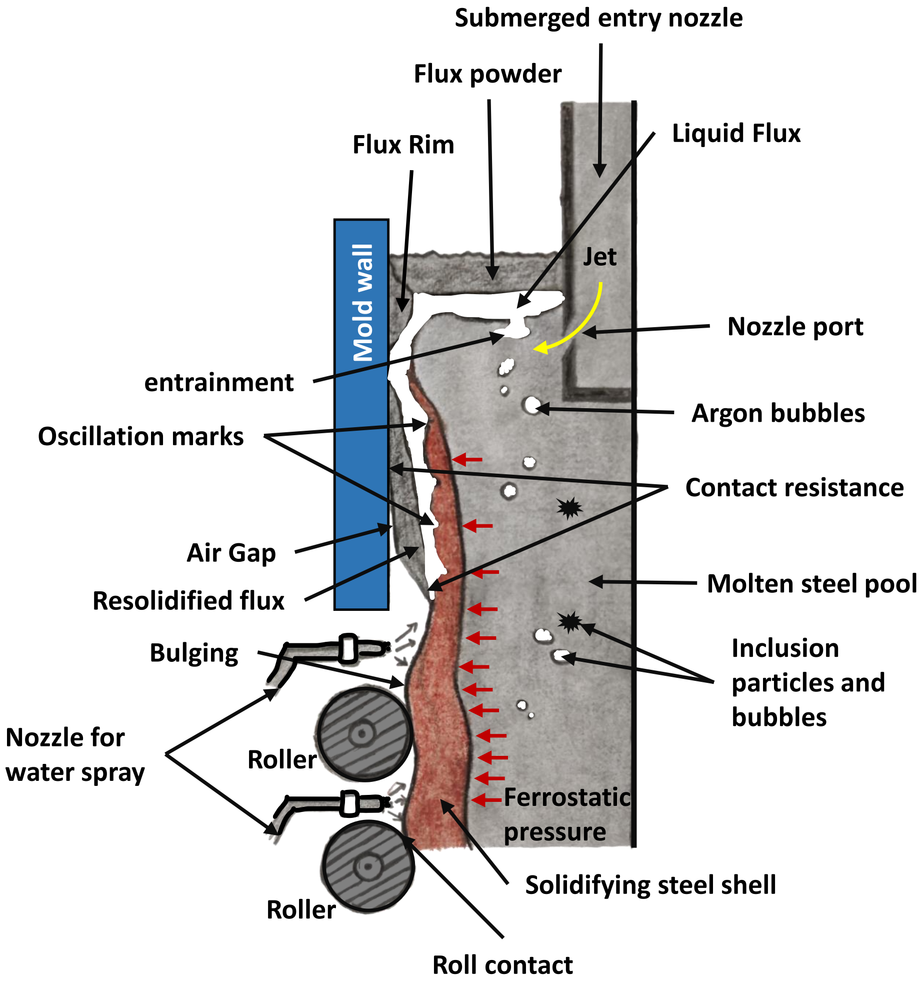

Figure 2.1. Flow Process in the Continuous Casting Mold for Molten Steel. The molten steel falls through the submerged entry nozzle. First, it solidifies at the mold wall, forming a solid shell around the liquid core. The rate of solidification depends on factors such as the mold temperature, casting speed, and heat transfer properties of the mold flux. As the solidification front advances, the liquid core shrinks in size, and the solid shell thickens. The mold is continuously cooled to maintain the desired shell thickness and prevent the formation of defects such as cracks or porosity. At the end of the mold, the solidified steel is withdrawn from the mold and enters the secondary cooling zone, where it is further cooled by water sprays or other methods to achieve the desired microstructure and mechanical properties. Finally, the solidified steel is cut to the desired length and prepared for downstream processing.

2.1.1. Role of Mold Flux in Continuous Casting Steel Industry. Continuous caster mold flux (CCMF) is a synthetic slag that is used in the continuous casting of steel. It plays an integral role in maintaining the stability and efficiency of the continuous casting process as it provides lubrication, controls heat transfer, absorbs nonmetallic inclusions, and prevents reoxidation of molten steel during continuous casting of steel. Mold flux helps reduce friction between the mold and the steel strand, and it also helps refine the steel by removing impurities. The role of mold flux in continuous casting steel process is depicted in Figure 2.1. Mold flux solidifies and shrinks during the casting process, which can lead to the formation of air gaps or voids between the mold and the steel strand if the shrinkage is not accounted for.

2.1.2. Effect of Mold flux Optimization. Measuring the air gap, thickness of the flux layer and the conductivity of mold flux can help with precise control of the injection amount of mold flux, which can improve the surface quality of steel. Additionally, measuring the melting temperature range and viscosity of mold flux can also help improve the quality of steel. Maintaining a constant thickness of the CCMF helps in achieving better surface quality of the cast steel and allows the use of lower superheat. A feasible electrode method has been proposed to measure the molten layer thickness of CCMF, which can help in controlling the injection amount of CCMF which improves the surface quality of cast product. In billet ultra-high-speed continuous casting molds, the thickness of mold flux film and air gap affects high-efficiency heat transfer, strand lubrication, and mold taper design, and measuring their thicknesses can aid in achieving optimal results. Thus, measuring the thickness of mold flux can help in achieving better quality of steel being cast.

2.2. INSTRUMENT AND EXPERIMENT DESCRIPTION

2.2.1. Brief Setup Details. Three EFPI sensors are instrumented and installed in a 3-part mold designed in-house. A wide wavelength band optical interrogator with a swept laser source and an enhanced photodetection module is connected to the sensors. Data acquisition software is developed using LabVIEW and MATLAB with proprietary real-time air gap and thickness estimation algorithm. The mold flux powder sample is placed in a graphite crucible and melted at 1400 ºC in a furnace and poured into the designed mold. The measured structural features such as air gap (formed due to shrinkage) and thickness are used to study and analyze crystallization, solidification, and shrinkage phenomena in 3 different mold flux samples. The chemical composition of the mold flux samples is also provided in the research done as part of publication.

2.2.2. Instrument Information. The EFPI interferogram is acquired from Hyperion SI-255 EV (enhanced visibility) optical interrogator manufactured by Micron-optics as shown below in Figure 2.1. It has an inbuilt swept laser source with a wide wavelength band of 160 nm and a laser sweep rate of 10 Hz.

Figure 2.2. Micron-optics Hyperion SI-255 EV Optical Interrogator. The Micron-optics Hyperion SI-255 EV optical interrogator was used to measure the real-time EFPI interferogram for the gap and thickness measurements in high temperature applications in this research. It has a 16-channel capacity and provides APIs (application programming interface) for developing data acquisition tools. It has a swept laser source with a sweeping rate of 10 Hz and a wavelength range of 1460 nm to 1620 nm.

2.3. SENSOR DESIGN AND CALIBRATION

2.3.1. Reason for Custom EFPI Design. In our ongoing research, we are conducting precise measurements of the gap formed during the shrinkage of molten CCMF, at a high temperature of 1400 ºC. However, commercially available EFPI sensors do not meet our requirements, as their design introduces measurement errors and an uncertain starting point for crystallization phenomena. This limitation poses a significant challenge to our research objectives, as accuracy and precision are paramount to our investigations.

2.3.2. Sensor Design with Internal Offset. To overcome the above challenge, we are designing custom EFPI sensors in-house with an internal offset between the cleaved end face of the fiber and the ferrule end through the ferrule hole shown in Figure 2.3. The fiber is held within the stainless-steel ferrule by means of superglue. However, care is taken to make this setup robust by means of high temperature resistant adhesive during experimentation. This design will enable us to obtain precise and reliable measurements of the gap and accurately identify the start point of crystallization phenomena. The internal offset design ensures that direct contact between the fiber end face and molten CCMF is avoided, reducing measurement errors caused by thermal expansion and stress on the fiber. Our custom-designed EFPI sensors will ensure that there is no uncertainty of the gap measurement when the experiment begins, providing a reliable starting point for observation of crystallization phenomena. Our work highlights the importance of developing specialized sensors that cater to specific research needs. By overcoming the limitations of commercially available sensors, we will advance our understanding of high-temperature materials and make significant contributions to the field of materials science.

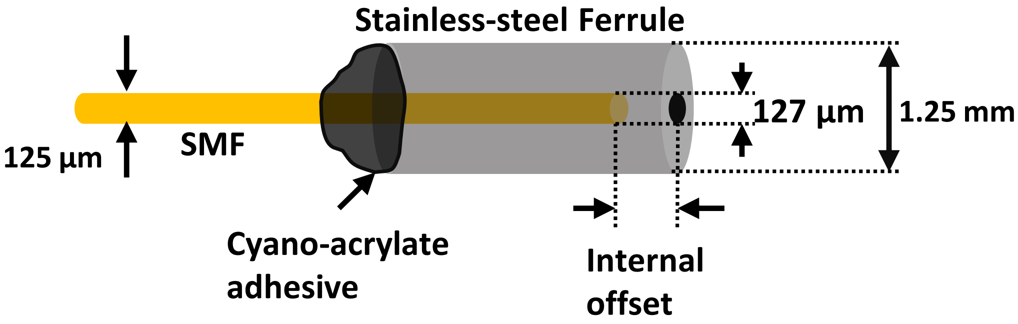

Figure 2.3. EFPI Sensor Design. The sensor was designed with internal offset intentionally to get reliability in measurement and certainty in observation of the crystallization phenomena of CCMF. This offset was compensated for in the data acquired.

2.3.3. Calibration of EFPI Sensor. Calibration was performed on the designed sensor up to 1mm with a micrometer to verify if appropriate gap measurement was obtained at the appropriate distances at room temperature. Calibration plot is shown in Figure 2.4.

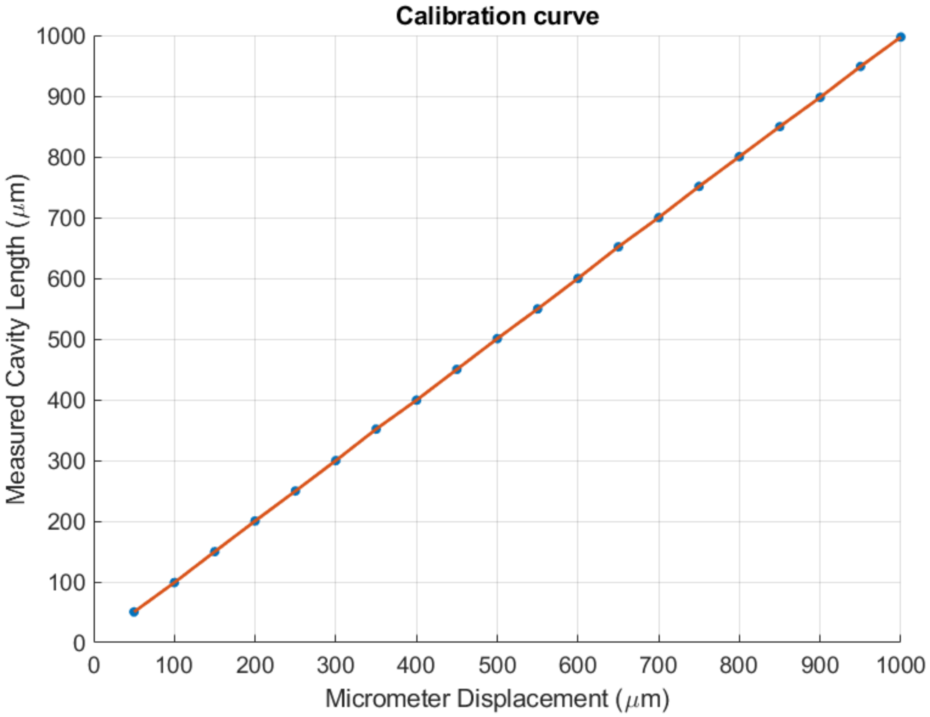

Figure 2.4. Calibration Curve of the EFPI Sensor. This plot compares the micrometer measured displacement with the cavity length measured by the designed sensor. It gives a straight line with slope of 0.9996 and angle of 44.9961°.

2.4. EFPI WORKING PRINCIPLE

2.4.1. Reflection from EFPI Cavity. When light is introduced into the EFPI sensor, it propagates along the optical fiber and is partially reflected at the cleaved surface. The reflected light then propagates back along the fiber and is partially reflected again at the same surface. This process results in the formation of a standing wave between the two reflective surfaces, with the reflected light waves interfering constructively and destructively. The interference pattern can be described mathematically using the Fabry-Perot equation:

$$I = I_1 + I_2 + 2\sqrt{I_1 I_2}\, cos[\Delta\phi + \phi_0] \tag{1}$$

where, I is the light intensity reflected by the entire EFPI cavity, I_1 is the light intensity reflected at the cleaved end face of the SMF, I_2 is the light intensity reflected by the external reflector formed when the molten CCMF is poured during the experiment, ϕ_0 is the initial phase difference and $\Delta\phi$ is the phase difference that corresponds to the optical path change and it is given by the equation:

$$\Delta\phi = \frac{4\pi(\Delta nl)}{\lambda_m} \tag{2}$$

where, λ_m is the wavelength of the source, n is the refractive index of the medium and l is the cavity length of the EFPI cavity.

2.4.2. EFPI Interferogram. The interference pattern represented by (1) produces a series of fringes as shown in Figure 2.5(b), with the spacing between the fringes dependent on the distance between the reflective surfaces shown in Figure 2.5(a). As the distance between the reflective surfaces changes, the fringe pattern shifts as shown in Figure 2.5(c) and Figure 2.5(d), allowing the EFPI sensor to be used to measure changes in distance as per equation (2).

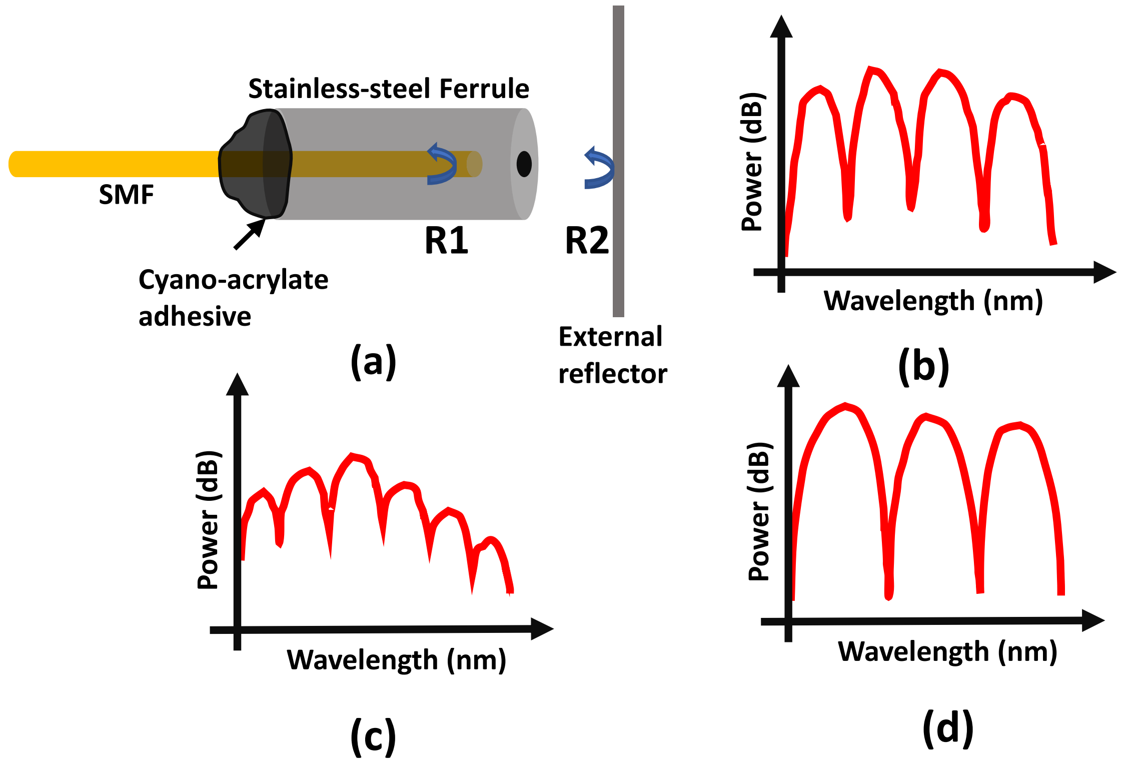

Figure 2.5. EFPI Sensor Working Principle. (a) EFPI sensor, reflected intensities when the external reflector manifests during the experiment. (b) interference pattern or the interferogram formed due to the light waves interfering constructively and destructively between the two reflectors. (c) Interferogram with more fringes and lower fringe depth due to increase in the cavity length. (d) Interferogram with less fringe and higher fringe visibility due to decrease in cavity length.

2.5. EFPI DEMODULATION ALGORITHM

This section presents the logical model of the low finesse EFPI demodulation algorithm. There are 4 stages to the developed algorithm which involve filtering, optimization, zero-crossing detection, and finally demodulation of the real-time acquired EFPI interferogram to extract cavity length information. This cavity length is ultimately estimated in real-time for various material science applications involving molten metal shrinkage that are involved in continuous casting processes. In the future, they have the potential to be used in crystal growth monitoring as well.

2.5.1. Spectrum Filter. The first part of the algorithm involves the application of a low-pass filter on the acquired EFPI interferogram. It is a custom two step low pass filtering process represented by the logic shown in Figure 2.6:

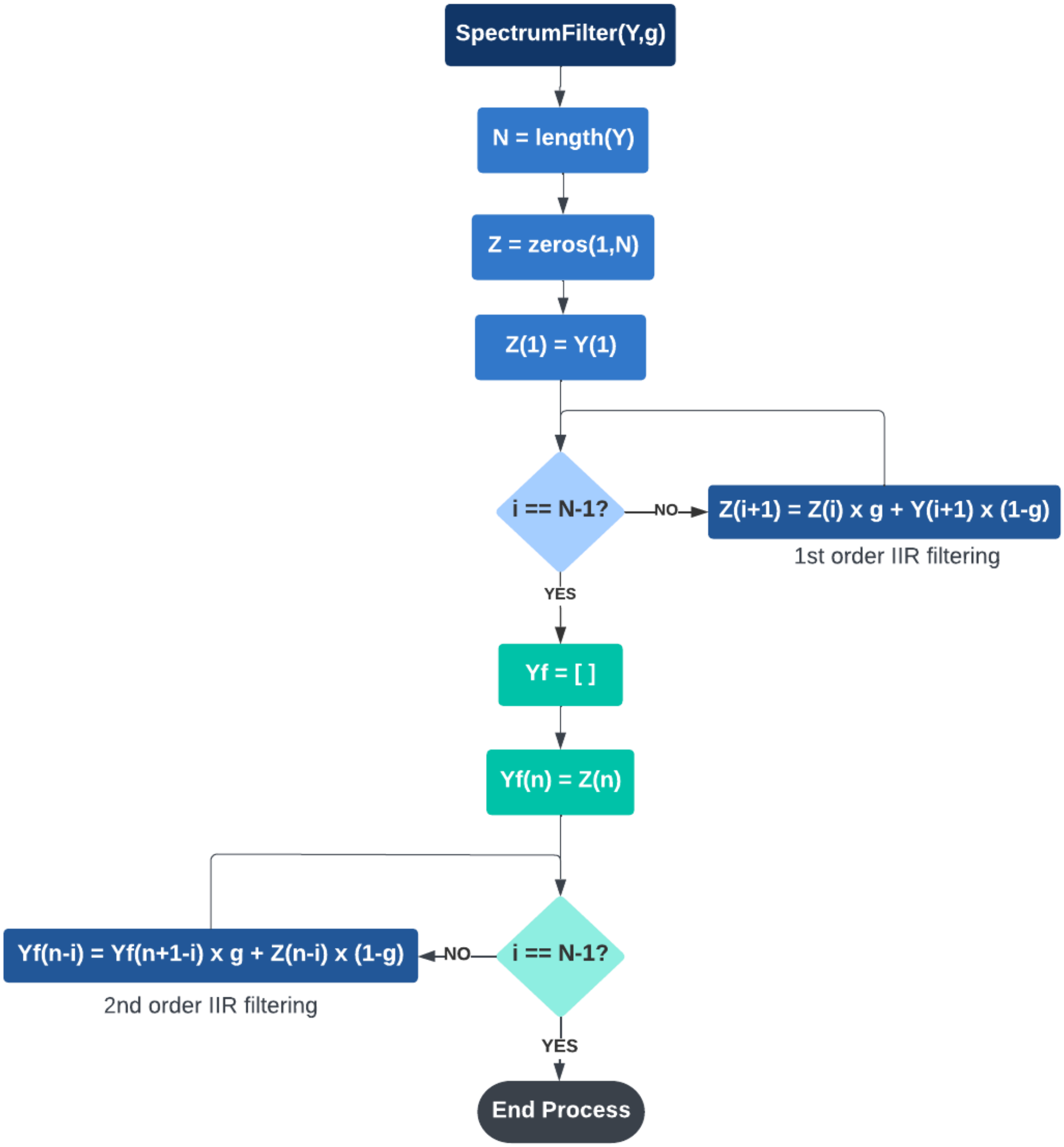

Figure 2.6. Flow Chart for SpectrumFilter Algorithm. The Flow Chart Describing the Process of "SpectrumFilter" Function Developed in MATLAB. This function takes in the EFPI interferogram "Y" and the filter coefficient "g" as input arguments and returns "Y_f" which is the filtered output interferogram. It performs a two-stage signal smoothing operation on the EFPI interferogram.

The second block from top calculates the length of the input signal vector “Y” and assigns it to the variable “N”. A new vector “Z” is created, which is the same size as “Y” and initially filled with zeros. The first value of “Y” to the first value of “Z”. The first loop applies a first-order IIR filter to the input signal “Y”. The output values of the filter are stored in the vector “Z”. The filter equation is a weighted sum of the previous filtered value “Z(i)” and the current input value “Y(i+1)”, with the weights determined by the filter coefficient “g” and its complement “1-g”. A new vector “Y_f” is created, which is initially empty, and assigns the last value of “Z” to the last element of “Y_f”. The second loop applies a second-order IIR filter to the output of the first filter (stored in “Z”). The output values of this filter are stored in the vector “Y_f”. The filter equation is similar to the first-order filter, but the current input value is replaced with the output value of the previous filter “Z(n-i)”, and the weights are determined by the same filter coefficient “g” and its complement “1-g”. By applying this two-stage filter, the output signal is a smoothed version of the input signal. This has reduced high-frequency noise and sharp changes. The amount of smoothing can be adjusted by changing the filter coefficient value passed into the function.

2.5.2. Optimization of Interferogram. The second part of the EFPI demodulation algorithm involves optimization of the interferogram. It applies the two-stage low pass (IIR) filtering to the interferogram multiple times with the logic shown in Figure 2.6. The “OptimizeSpectrum” function applies a series of smoothing filters to the input signal “Y” to remove noise and reduce high-frequency components, and then calculates an optimized signal by subtracting the final filtered signal from the original filtered signal and scaling the result to a range of -100 to 100 as depicted in Figure 2.7. The resulting optimized signal is smoother and easier to analyze than the original input signal. The filter coefficients used in the function can be adjusted to control the amount of smoothing applied to the signal.

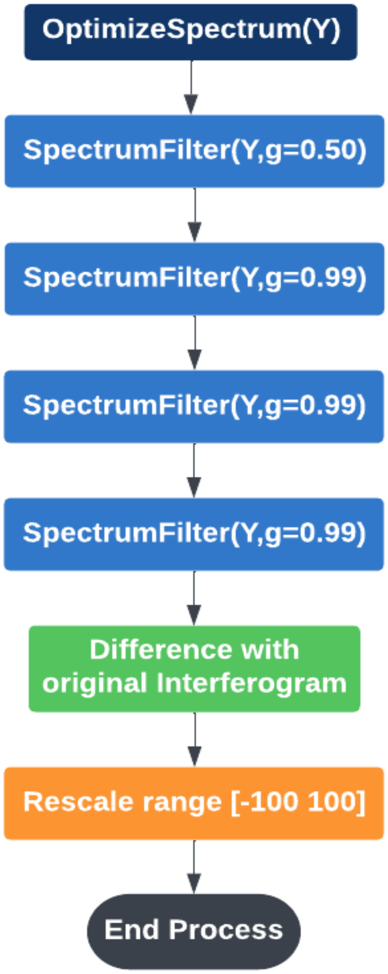

Figure 2.7. Flow Chart for OptimizeSpectrum Algorithm. The flow chart describes the process of “OptimizeSpectrum” function developed in MATLAB. This function takes in the filtered EFPI interferogram “Y” and returns an optimized output interferogram. It performs multiple “SpectrumFilter” operations and returns a rescaled interferogram between the range [-100 100].

2.5.3. Zero-Crossing. The third part of the EFPI demodulation algorithm operates on the optimized interferogram to perform custom zero-crossing detection with the logic shown in Figure 2.8.

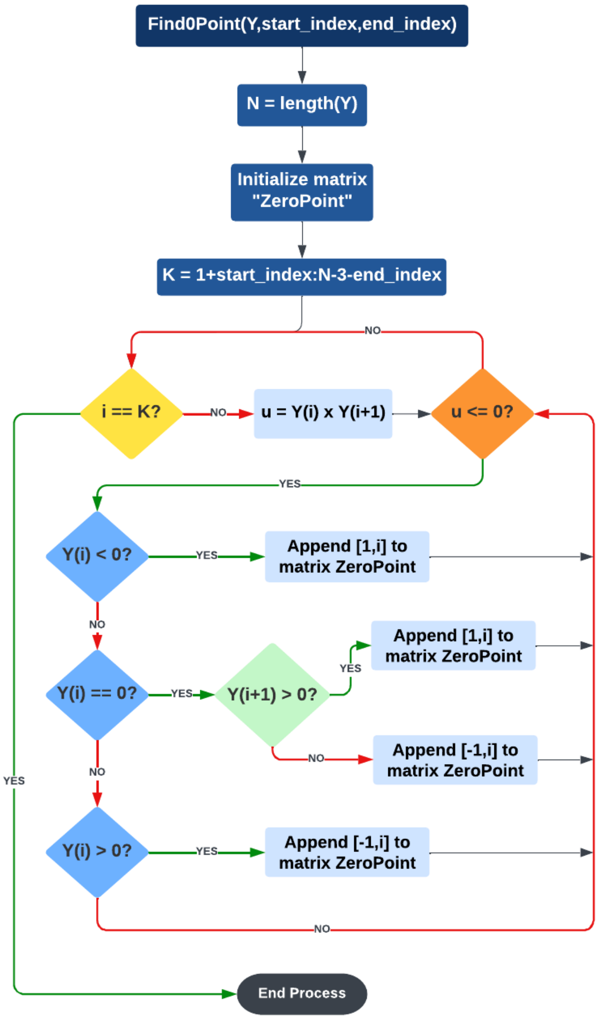

Figure 2.8. Flow Chart for Find0Point Algorithm. The flow chart describing the process of "Find0Point" function developed in MATLAB. This function takes in the optimized EFPI interferogram "Y" and returns a normalized output zero-crossing detected signal.

The "Find0Point" function finds the zero-crossings in the input signal "Y" by iterating over its indices and checking if the product of the values at adjacent indices is less than or equal to zero. The direction of the zero-crossing is determined by the sign of the value of "Y" at the index, and a matrix called "ZeroPoint" is created to store the indices and directions of the zero-crossings. The "start_index" and "end_index" arguments can be used to crop data points from the beginning and end of the signal, respectively. Finally, the zero-crossing signal is used to estimate the cavity length of the EFPI cavity. This is shown in Figure 2.9. The “DemodulationEFPI” function takes in the wavelength “lambda” and the EFPI interferogram “Y” as inputs and returns the calculated cavity length “L” of an EFPI cavity. The function applies several filtering and normalization steps to the interferogram, finds the zero-crossings, calculates the positions of the peaks and zero-crossing polarity, and then uses these positions to calculate the accurate cavity length $\boldsymbol{L}$ using equation shown below. This length is divided by the appropriate refractive index of the medium to (1.000293 for air) separate the real cavity length from the optical path difference:

$$L(n) = \begin{cases} \frac{\lambda_{zp}(\lceil k \rceil + 2)}{4}, & ZeroPoint2(n,1) == 1 \wedge mod(k,2) \leq 1 \\ \frac{\lambda_{zp}(\lceil k \rceil - 1)}{4}, & ZeroPoint2(n,1) == 1 \wedge mod(k,2) > 1 \\ \frac{\lambda_{zp}(\lceil k \rceil)}{4}, & ZeroPoint2(n,1) == -1 \wedge mod(k,2) \geq 1 \\ \frac{\lambda_{zp}(\lceil k \rceil + 1)}{4}, & ZeroPoint2(n,1) == -1 \wedge mod(k,2) > 1 \end{cases} \tag{3}$$

where, $\boldsymbol{\lambda_{zp}}$ is the wavelength of light in the cavity at the position of the nth zero crossing in nanometers. $\boldsymbol{ZeroPoint2(n, 1)}$ is the matrix that contains zero-crossings. $\boldsymbol{k}$ is given by the below equation:

$$\boldsymbol{k = \frac{4l}{\lambda_{zp}}} \tag{4}$$

where, $\boldsymbol{l}$ is the approximate cavity length estimated by the stage-1 shown in Figure. 2.9.

2.5.4. Estimating the Accurate Cavity Length. The “DemodulationEFPI” function is called within the LabVIEW Data Acquisition (DAQ) software developed in-house using Hyperion SI255 optical interrogator’s APIs. This software is used to acquire interferogram and process to obtain cavity length/gap measurements of CCMF in real-time during its crystallization and solidification phenomena.

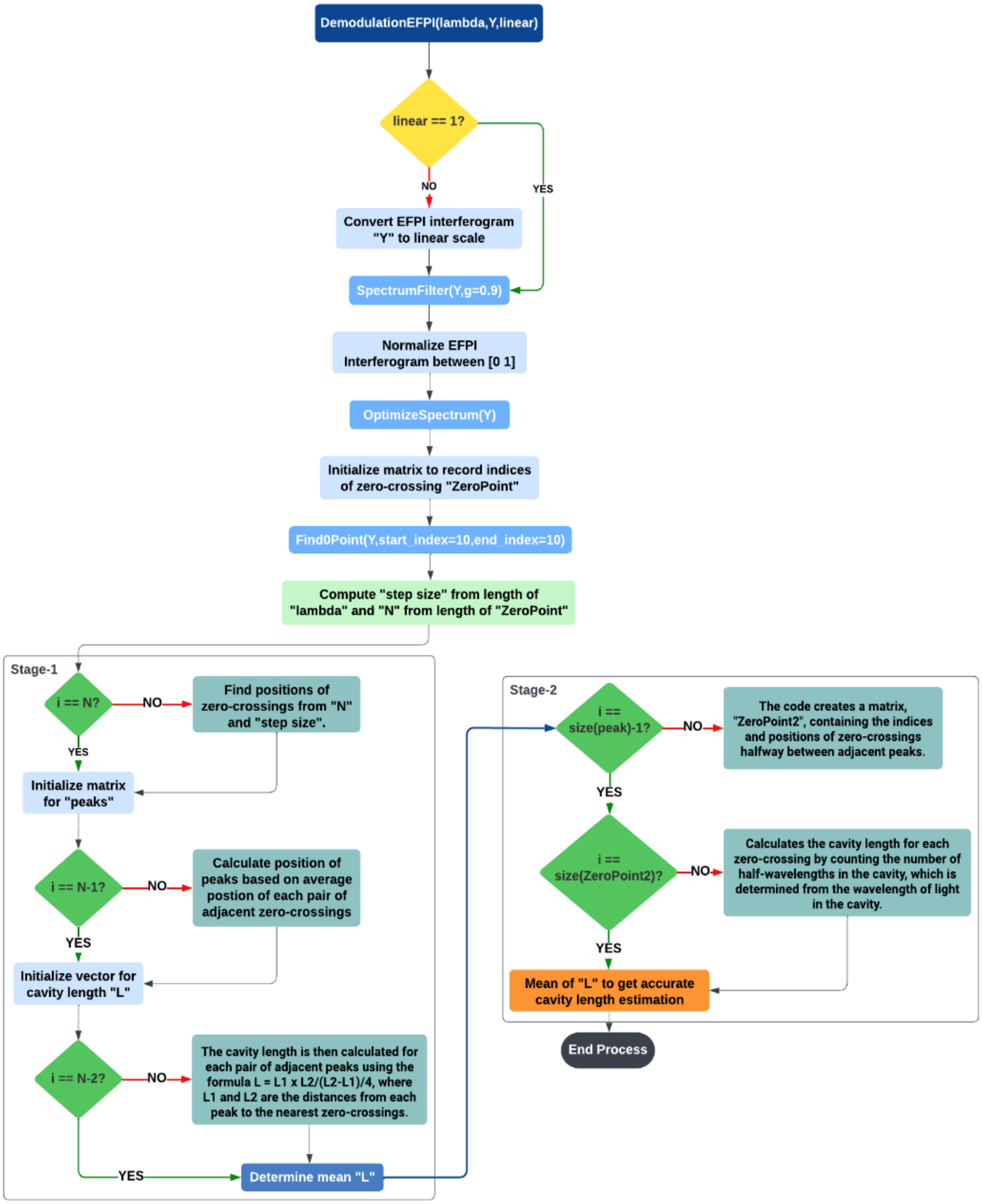

Figure 2.9. Flow Chart for DemodulationEFPI Algorithm. The flow chart describes the process of “DemodulationEFPI” function developed in MATLAB. This function takes in the optimized EFPI interferogram “Y” with wavelength and returns the accurate estimate of the EFPI cavity length by using the zero-crossing detection.

PAPER

I. REAL-TIME AIR GAP AND THICKNESS MEASUREMENT OF CONTINUOUS CASTER MOLD FLUX BY EXTRINSIC FABRY-PEROT INTERFEROMETER

ABSTRACT

Mold Flux plays a critical role in continuous casting of steel. Along with many other functions, the mold flux in the gap between the solidifying steel shell and the mold serves as a medium for controlling heat transfer and as a barrier to prevent shell sticking to the mold. This manuscript introduces a novel method of monitoring the structural features of a mold flux film in real-time in a simulated mold gap. A 3-part stainless-steel mold was designed with a 2 mm, 4 mm and, 6 mm step profile to contain mold flux films of varying thickness. An Extrinsic Fabry-Perot Interferometer (EFPI) was installed at each of the three steps in the mold. Mold flux was melted in a graphite crucible at 1400 ºC and poured into the instrumented step mold for analysis. Interferograms from the three EFPIs were acquired and processed in real-time to measure the air gap and thickness of each flux film during solidification. Measurements were performed on two different mold flux compositions. Results demonstrate that the proposed system successfully records structural features of the flux film in real-time during cooling. In addition, the measurement method has potential to monitor crystal nucleation and growth in a variety of crystallizing glass systems. This type of EFPI based real-time gap measuring scheme has lot of potential in steel industries, biomedical, and civil engineering applications.

Index terms – Mold flux, Basicity, Extrinsic Fabry-Perot Interferometer (EFPI), Interferogram, Air gap, Thickness measurement, Single-mode fiber (SMF), Real-time measurement.

1. INTRODUCTION

Mold flux is an engineered calcium silicon oxyfluoride glass that is designed with a target viscosity and crystallization behavior for the use as a lubricant in the continuous casting process. Mold flux is often spray dried and carbon coated to control its melting behavior in the mold [1] and a liquid layer of the flux develops on steel surface and then enters the mold gap around the mold perimeter. Mold flux has several functions, such as protection of molten steel from oxidation [2], heat removal control, during initial steel shell formation [3], absorption of nonmetallic inclusions [4], lubrication of the solidifying steel strands during extraction, and thermal insulation [5]. If the mold flux has a high degree of crystallinity, the steel shell that exits the mold can be excessively thin, leading to shell bulging, due to the shell's inability to withstand the ferrostatic pressure of the internal molten steel [6]. Furthermore, during the casting process, mold flux aids in absorption of non-metallic inclusions in steel [7], and as such, the flux can experience composition changes that affect flux viscosity and crystallization behavior. Studying the structural properties of mold flux in mold gap can provide new insights into the prevailing flux film heat transfer, mold interface contact resistance and their links to crystallization behavior. An efficient way of measuring air gap and flux film thickness for several continuous casting mold fluxes during cooling and solidification is presented in this research.

Crystallization is defined as the process by which a liquid or short-range order glass transforms to an ordered crystal structure, such that overall energy of the system is minimized [8-10]. Nucleation occurs at the onset of crystallization when the atoms or molecules of molten flux arrange themselves to form crystals of a critical size to support thermodynamically stable growth [11]. Nucleation rate is important in determining crystalline structure and grain size [12] in the flux film. In the continuous casting process, the liquid flux enters the mold gap at the mold perimeter and the portion of the flux that contacts the mold is rapidly cooled to form a glass. The molten flux undergoes a wide range of cooling conditions under which crystallization is promoted and crystal nuclei will form and grow. While the flux nearest to the hot steel remains liquid, other parts of the flux film exhibit a range of cooling conditions that can either promote direct crystal formation from the liquid or crystallization from the glass. This process is difficult to study, making EFPI a great candidate for the proposed sensor solution [13]. The flux also undergoes thermal contraction as it cools, which results in shrinkage [14]. Shrinkage can cause the flux to pull away from the mold wall, increasing resistance to heat flow at the interface. Cracks can also form in the flux film as it contracts if the surface of the mold becomes too rigid to accommodate internal shrinkage [15]. The overall flux film thickness and the thickness of the air gap between the flux film and the mold wall is a consequence of this shrinkage.

Several methods have been used in heat transfer simulations of the continuous casting mold to predict or calculate the flux film air gap and thickness during molten flux solidification [16,17]. However, to date, air gap and flux thickness have not been measured in-situ during flux solidification, and instead, flux film surface roughness, thickness, and temperature profile measurements across mold gap have been used to estimate these parameters. The mold flux serves several primary functions in the continuous casting of the steel as discussed earlier. Hence, measurements of the air gap and flux film thickness are relevant because they provide information that directly impacts the quality of steel being manufactured. Mold fluxes exhibit both glassy and crystalline phases during cooling [18]. For this reason, it is important to understand the effects of these structures on interfacial gap development and mold flux film thickness and their relationships to mold heal removal.

Fiber optics are very suitable for highly sensitive measurements [19-21]. They have several advantages including electromagnetic immunity, lightweight, flexibility, and compact size [22-25]. They are also capable of multiplexed and distributed measurement where continuous physical quantity mapping is required, such as temperature and strain [26,27]. Fiber optic sensors can detect optical path differences as small as 1 nm when configured as interferometers [28]. In this research, Extrinsic Fabry-Perot Interferometry (EFPI) is used as a point sensor for gap measurement. The EFPI can detect reflections from multiple reflective interfaces through modulated interferometry [29], which makes it very suitable for this application. It is necessary to periodically tune the optical wavelength of the source with a wide wavelength band for mold flux applications. Hence, it is tuned through a relatively large range such as ~100 nm at a sweep rate of 10 Hz or 100 Hz [30]. This cannot be performed using conventional tunable laser source. A swept laser operates by rapidly changing the instantaneous frequency of the laser output, which is extensively used to interrogate fiber optic sensors [30-32] such as in measuring temperature and strain from Fiber Bragg Grating (FBG) sensors [33]. It is also used in EFPI interrogation for acoustics [34] and refractive index [35] sensing.

To summarize, three EFPIs were instrumented and installed in a 3-part custom designed mold. The sensors were connected to a wide wavelength band optical interrogator with a swept laser source and an enhanced photodetection module. Data acquisition software was developed in LabVIEW using in-house designed real-time air gap and thickness estimation algorithms. The flux sample was heated and melted in a furnace and then poured into the 3-part mold. The measured EFPI signals were used to document and analyze solidification and shrinkage phenomena in 2 different flux samples.

2. SENSOR, MOLD DESIGN AND EXPERIMETAL SETUP

2.1. SENSOR DESIGN

(a) EFPI sensor design

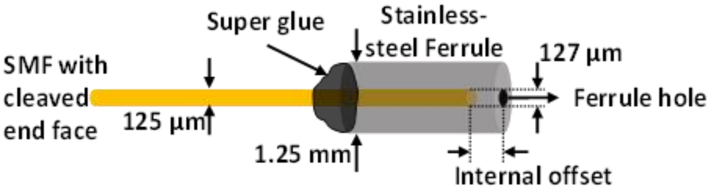

(b) EFPI fabrication and calibration

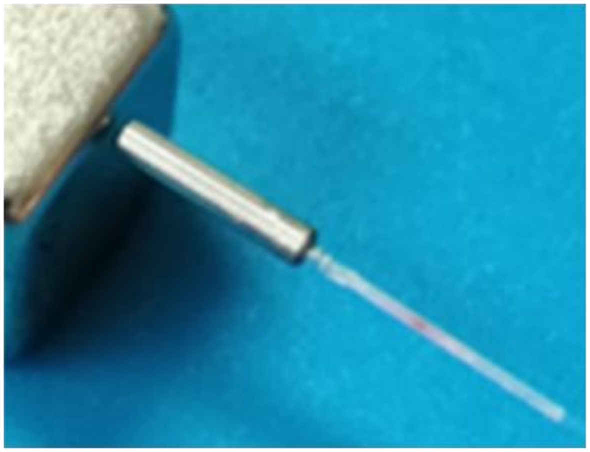

Figure. 1 Instrumentation of EFPI sensor. (a) SMF having cleaved end face is inserted into a stainless-steel ferrule with internal offset for point gap and thickness measurement. (b) fabrication of EFPI and measuring internal offset/calibrating with a magnet.

Three EFPIs were instrumented in a very simple manner. A single-mode fiber was cleaved and inserted into a stainless-steel ferrule having an outer diameter of 1.25 mm. The hole in the stainless-steel ferrule had and inner diameter of 127 µm which holds the SMF with cleaved end face. The fiber end face was not flush with the end of the ferrule. This was done intentionally to have an internal offset such that the point at which molten flux starts to solidify can be clearly detected and to prevent direct contact of molten flux with the fiber end face. Care was taken to ensure that the internal offset did not exceed 200 µm, which would have adversely affected the quality of the measurement. Instrumentation of the EFPI is shown in Figure 1.

Table 1. EFPI Internal Offsets

EFPI SENSOR	**INTERNAL OFFSET (µm)**
TOP	100
MIDDLE	50
BOTTOM	130

Table 1 shows the offset or the distance by which the cleaved end face of the SMF is inset from the stainless-steel ferrule’s hole. 3 EFPIs were instrumented, and they were calibrated using a highly reflective magnetic surface for measuring the internal offsets. This is done to prevent penetration of molten flux sample into sensor. These distances do not interfere with measurement as they are compensated for the real-time determination of thickness and air gap. The point gap sensor is a single-mode fiber of 1550BHP – 0.13 NA (numerical aperture), having an operating wavelength range of 1460 nm – 1620 nm. The fiber had a diameter of 125 µm and was protected by a FT900W polymer tubing.

2.2. MOLD DESIGN AND INSTRUMENTATION

A 3-part mold was designed for the purpose of measuring the air gap and thickness of molten mold flux. For ease of EFPI installation, the mold was designed to have 3 parts as shown in Figure 2. The front-plate of the mold was designed to have an opening at the bottom. This allows the molten mold flux sample to flow through the mold with minimal friction and simultaneously have contact with all three step profiles of the mold.

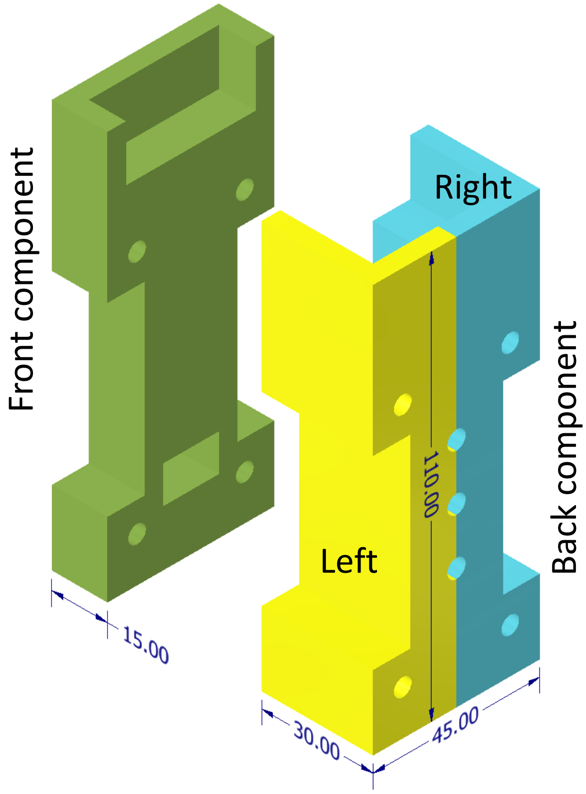

Figure 2. Mold design and specifications. This figure illustrates the design of a 3-part mold used for mold flux analysis. It has a dimension of (110×45×45) mm when combined.

The front component is a plane wall from which light from the EFPIs are reflected and its design and dimensions are shown in Figure 3(a). The back component of the mold is split into 2 parts having step profile of 2 mm, 4 mm, and 6 mm. Its design dimensions are shown in Figure 3b and Figure 3c.

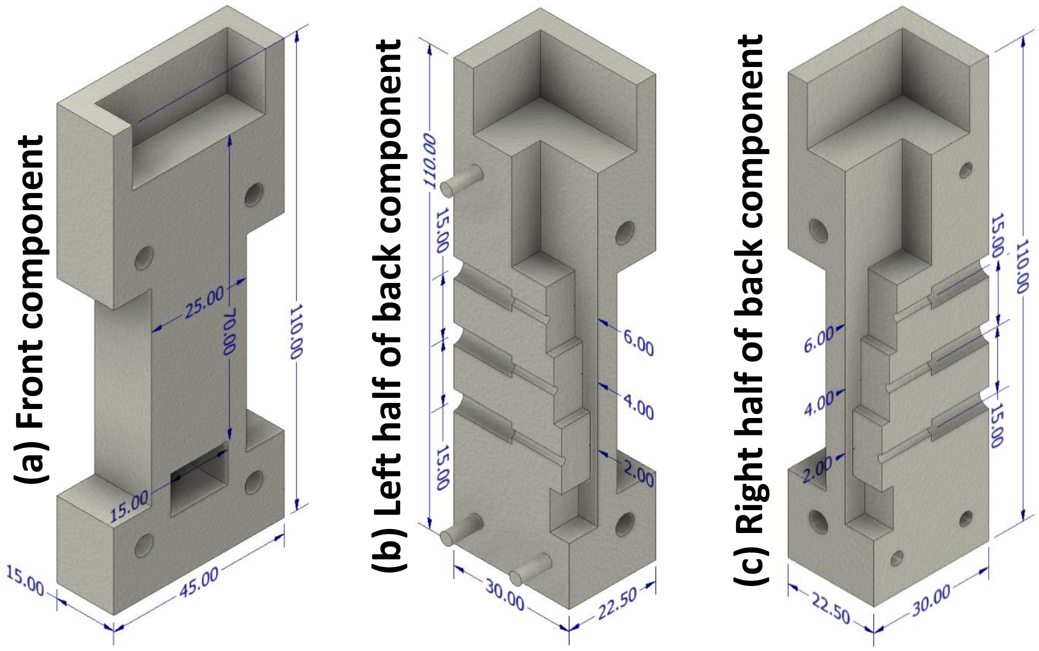

Figure 3. Flux mold specifications and dimensions. a) shows the dimensions of the front component, its interior has a smooth finish for good reflectivity. b) cross-section, left half of flux mold with the step profile. c) cross-section, right half of flux mold with the step profile.

These two mold parts have groves in the center such that, when they are joined, they form holes of 1.27 mm inner diameter while retaining the step profile. The holes are used to house and clamp the EFPI ferrules containing the SMF. The EFPIs were installed in the grooves on the left side of the back component with cyanoacrylate adhesive. The right side of the back component was combined with the opposite half of the mold to provide an enclosure and to affix the ferrules in place. Both parts of the back component were held together with bolts. The front mold component was placed in contact with the back components such that all the EFPIs are exactly perpendicular to the wall. The fibers extending from the EFPI sensors were protected by thin stainless-steel tube, that protrude from the back of the mold. The mold is shown after installation of the EFPIs in Figure 4. The stainless-steel tubes are firmly attached to the back of the mold by means of a high temperature adhesive which was cured with a torch. The sensors were then connected to an optical interrogator controlled by computer.

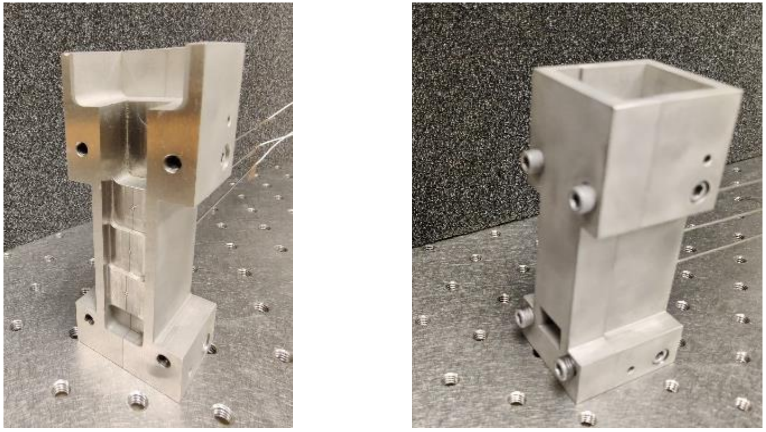
(a) Back part of mold with EFPIs instrumented

(b) Complete mold setup – front view

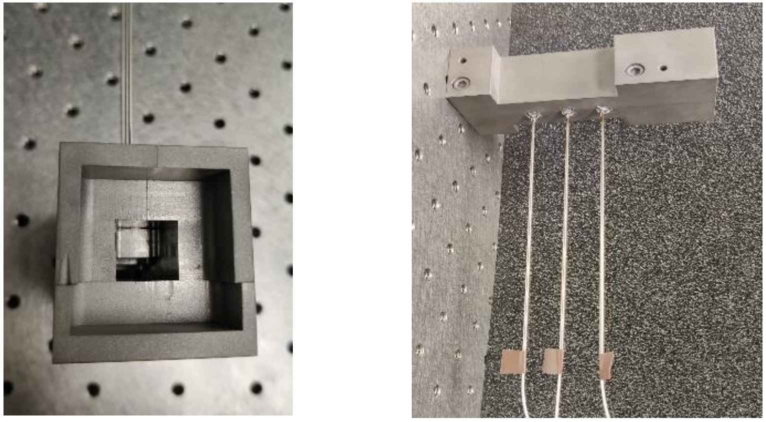
(c) Complete mold setup – top view

(d) Stainless-steel tube shielding of the SMF cables

Figure 4. Flux mold, EFPI sensors installed with shielding. a) shows the back components of the mold and point gap sensors after EFPI installation, step profile can be observed. b) the front component bolted to the back components after EFPI installation such that the wall is facing the sensor. c) Top view of the mold setup, where the synthetic molten flux sample is poured. d) Stainless-steel tubing protection to the SMF cables coming out of the back side of flux mold.

2.3. EXPERIMENTAL SETUP

The experimental setup shown in Figure 5 consists of instrumented mold, optical interrogator, computer to acquire data from the optical interrogator, heating furnace with temperature controller and graphite crucible in which powdered mold flux was poured. First, the instrumented mold was placed on a firm stable platform with the stainless-steel tubes covered by heat resistant foam. The single-mode fibers of the 3 EFPIs were connected to a Micron-Optics Hyperion SI-255 enhanced visibility optical interrogator. The Hyperion SI-255 is a 16-channel optical instrument with a swept laser operating at a 10 Hz sweeping rate. It has a very broad wavelength band of 160 nm, from 1460 nm to 1620 nm.

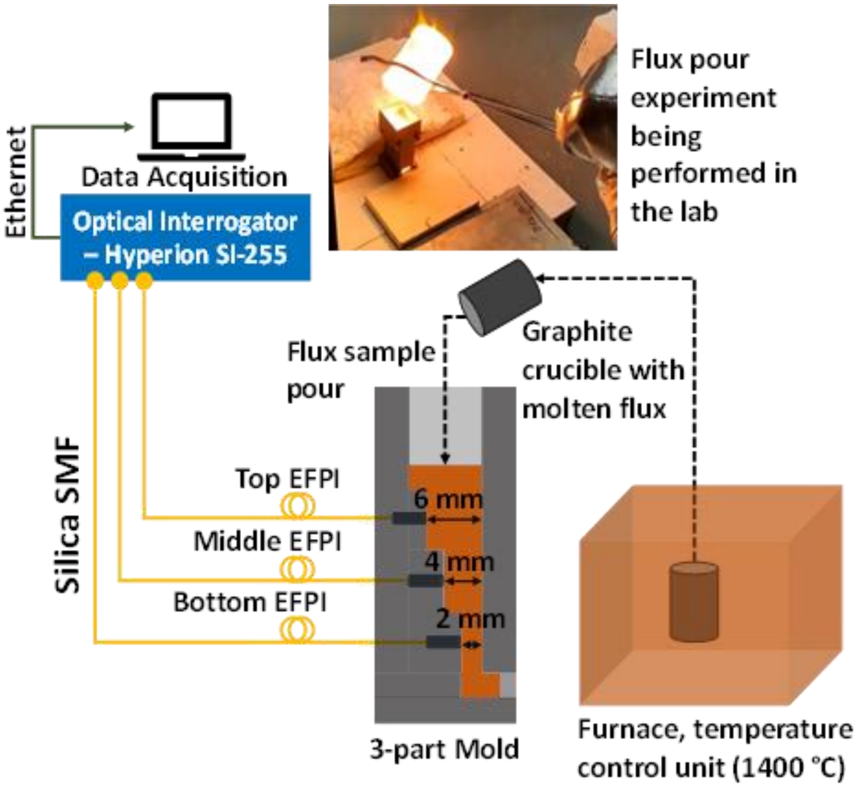

Figure 5. Experimental setup for measuring air gap and thickness of synthetic mold flux with a real-time optical interferogram acquisition. The graphite crucible with mold flux is heated to 1400 ºC in a furnace and poured into the instrumented mold for measuring thickness and air gap. The sensors were protected with stainless-steel tubes and covered with heat resistant polymer.

An empty graphite crucible was preheated to 1400 ºC in the furnace. A granular mold flux sample was poured into the graphite crucible and placed in the furnace. The flux sample was then melted at 1400 ºC in the furnace. At this point, the data acquisition was initiated on the computer connected to Hyperion SI-255. The graphite crucible with molten flux sample was quickly removed from the furnace and poured into the instrumented mold. As the sample started to crystallize and solidify, there were multiple cavities formed between the fiber end face inside the stainless-steel ferrule and the interior part of front component of the mold wall, resulting in complex EFPI pattern. This resulted in an interferogram with varying Free Spectral Range (FSR) measured by the Hyperion SI-255. This spectrum was processed in real-time to obtain the structural features of the flux during cooling and solidification of the flux. An FFT of the spectrum was obtained to identify the different cavity reflections in the system.

2.4. MEASUREMENT THEORY

As soon as the molten flux was poured into the mold, it started to solidify and shrink. The resulting shrinkage caused an air gap to form between the EFPI sensor and the flux surface facing the EFPI. A second reflection was also sometimes observed from the opposite wall, depending on its distance across the mold cavity and the transparency of the flux film. As flux solidification progresses, several reflectors begin to form within the flux which can be represented as $R = R_1, R_2, \dots, R_n$. These reflections are due to the formation of air bubbles which result from the inadequate mixing, excessive turbulence, and trapped gases within the mold flux in continuous casting. This phenomenon is time and temperature dependent. The measurement was performed for a period of ~5 min to keep consistency across both samples. Additionally, crystallinity of the mold flux is dependent on its chemistry [36,37]. Hence, 2 different flux samples were tested. An example of the multiple reflections that can form during solidification of the mold flux is depicted in Figure 6.

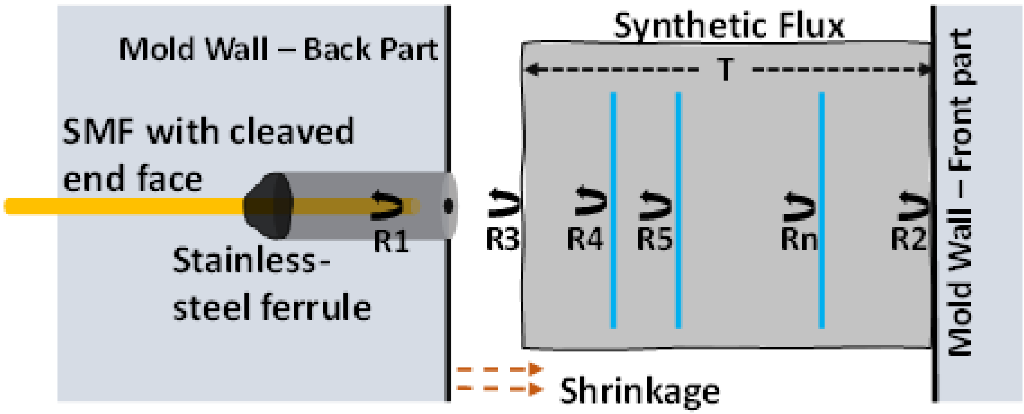

Figure 6. Measurement of air gap and thickness of flux undergoing crystallization and solidification. The flux shrinks due to crystallization and solidification causing an air gap. Multiple reflectors form within the flux due to entrapment of air bubbles which aid in the analysis of the flux material. (R_2, R_3) reflectors can be used to determine the flux thickness.

Shrinkage from the back side of the mold is significantly larger than the shrinkage from the front side. This is due to more rapid heat loss from the back of the mold due to the mold wall thickness. Thus, shrinkage from the back of the mold dominates air gap formation. The light intensity reflected from the air gap R_{ag} formed by the cavity due to reflectors (R_1, R_3) is given by:

$$R_{ag} = R_1 + R_3 + 2\sqrt{R_1 R_3}\, cos\left[\Delta\varphi_{ag} + \varphi_0\right] \tag{1}$$

where, φ_{ag} is the phase difference due to the cavity length l_{ag} of the air gap given by equation (2) and φ_0 is the initial phase:

$$\Delta\varphi_{ag} = \frac{4\pi\,\Delta(n_a l_{ag})}{\lambda_m} \tag{2}$$

where, λ_m is the wavelength of the source and $n_a = \sim 1$ is the refractive index of air. Similarly, the light intensity reflected by the total mold gap with molten flux inside is given by an equation obtained from Fast Fourier Transform (FFT) analysis of the modulated interferogram:

$$R_{mg} = R_1 + R_2 + 2\sqrt{R_1 R_2}\, cos\left[\Delta\varphi_{mg} + \varphi_0\right] \tag{3}$$

where, R_{mg} is light intensity reflected by the mold gap as shown in Figure 6, which is between reflectors (R_1, R_2) and φ_{mg} is the phase difference due to the cavity length l_{mg} between the reflectors (R_1, R_2) given by:

$$\Delta\varphi_{mg} = \frac{4\pi\, \Delta(n_g l_{mg})}{\lambda_m} \tag{4}$$

where, n_g is the group refractive index of the molten mold flux and air gap. The light intensity reflected from the mold flux sample, i.e., between the reflectors (R_3, R_2) can be expressed by the equation:

$$R_f = \; R_3 + R_2 + 2\sqrt{R_3 R_2}\, cos\left[\Delta\varphi_f + \varphi_0\right] \tag{5}$$

where, R_f is light intensity reflected only by the mold flux shown in Figure 6. The corresponding phase change can be represented by the expression:

$$\Delta\varphi_f = \frac{4\pi\, \Delta(n_f l_f)}{\lambda_m} \tag{6}$$

where, φ_f is the phase difference due to the cavity length l_f between the reflectors (R_3, R_2) and $\mathrm{n_f} = \sim 1.52$ is the refractive index of the mold flux which is assumed to be constant throughout. The optical path length $(\mathrm{n_g} l_{\mathrm{mg}})$ in (4) is given by:

$$n_g l_{mg} = \; n_a l_{ag} + n_f l_f \tag{7}$$

The thickness of flux l_f or T can be estimated by rewriting equation (7) as:

$$T = l_f = \frac{n_g l_{mg} - l_{ag}}{n_f} \tag{8}$$

The distance of air bubbles within flux from the EFPI sensor or flux surface can be calculated, as the flux undergoes solidification. As shown in the Figure 6, when reflector R_4 is formed, another cavity with reflectors (R_1, R_4) manifests. The light intensity reflected from this cavity is given as:

$$R_c = R_1 + R_4 + 2\sqrt{R_1 R_4}\, cos[\Delta\varphi_c + \varphi_0] \tag{9}$$

where, R_c is the reflected light intensity which can be obtained from FFT of modulated spectrum and φ_c is the phase difference due to the cavity length variation from reflector R_4. This cavity length l_c can be calculated by:

$$\Delta\varphi_c = \frac{4\pi\, \Delta(n_g l_c)}{\lambda_m} \tag{10}$$

where, l_c is the distance of the air bubble within flux from the EFPI sensor or mold wall as shown in Figure 6 and n_g is the group refractive index of air gap and the flux film. The time varying air gap, thickness of the flux and distance of air bubble within flux from the EFPI sensor can be measured in real-time and example results are included in the following section.

3. SPECTRUM ACQUISITION AND DATA PROCESSING

3.1. DATA ACQUISITION AND PROCESSING

An interferogram is acquired by Micron-Optics Hyperion SI-255 optical broadband interrogator. At each time interval, an interferogram of 20000 points is obtained having a wavelength band of 1460 nm to 1620 nm. This spectrum was fed to an in-house developed low finesse EFPI demodulation algorithm to estimate the air gap in real-time. Data were acquired for 330 seconds (~5 mins) on average for 2 flux evaluations.

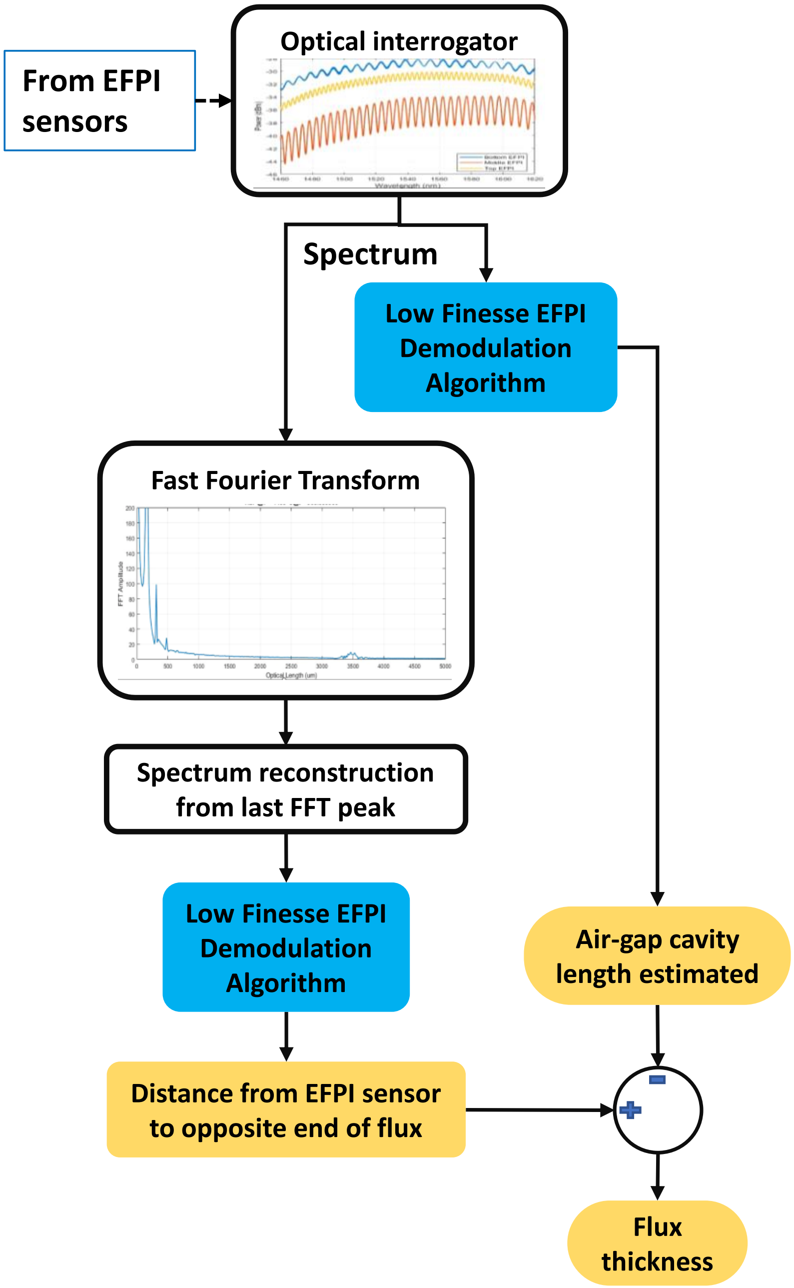

Figure 7. Data acquisition and processing. Spectra are acquired in real-time from the optical interrogator and processed to obtain the air gap and FFT. The last peak is used for spectra reconstruction and demodulation to obtain the distance between EFPI sensor and the opposite end of the flux. The subtraction of measured air gap from this yields the flux thickness measurement.

FFT of the spectra was obtained from which multiple peaks were identified near the shorter and longer optical lengths. This indicates the presence of several trapped air bubbles within the flux separate from the air gap. The largest FFT peak after DC component corresponds to the air gap. The subsequent peaks next to air gap peak correspond to the reflections from within the flux due to the trapped air bubbles. The DC component of the FFT signal is the DC offset (always real for a real signal) that pertains to the 0 µm optical path length. The right most peak corresponds to the reflection from opposite mold wall. From the FFT data, the last or right most peak is considered and a new spectrum is constructed and processed with the EFPI demodulation algorithm. The distance from EFPI sensor to the opposite end of the flux is measured and subtracting the air gap provides the thickness of the mold flux. The distance of trapped air bubbles within flux from EFPI sensor are measured in a similar fashion. The data acquisition and processing flow is shown in Figure 7. It uses the in-house developed low finesse EFPI demodulation algorithm to determine the air gap and thickness.

3.2. LOW FINESSE EFPI DEMODULATION ALGORITHM

Using equations (2), (4) and (8), the respective cavity lengths can be estimated. However, directly doing so will result in very poor resolution for larger cavity lengths. This means that the effective measurement range of the EFPI system becomes less accurate. To extend this measurement range to larger distances, an advanced signal processing method involving zero-crossing and spectrum reconstruction is used. The EFPI demodulation flow chart is included as Figure 8.

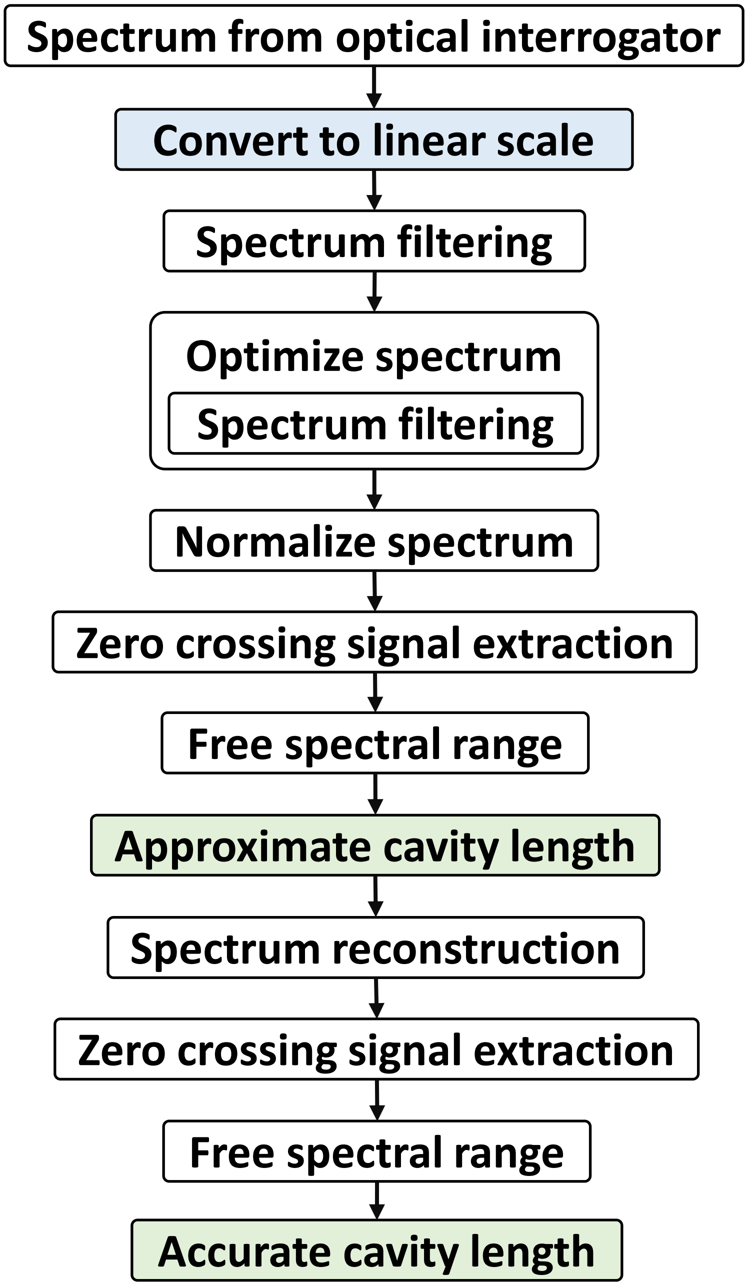

Figure 8. Low Finesse EFPI demodulation algorithm flow chart. Two step demodulation process with zero crossing signal analysis and spectrum reconstruction for accurate determination of the air gap. For determining thickness, the algorithm was used to estimate the mold gap from the FFT spectra, which was subtracted from the air gap.

This algorithm can achieve cavity length that was measured with high resolution (~1 nm) in the lab environment. This is possible only on an optical table and with a perfect external reflector such as a silicon wafer. But the algorithm performs reasonably well in an environment with disturbances and gives a reasonable resolution of 0.1 µm ± 10 nm when determining cavity length. This makes it quite suitable to measure the structural features of the mold flux in real-time. The code for this algorithm was developed in LabVIEW tool. This sub-VI was used as a function call in the main real-time data acquisition program developed in LabVIEW. It takes in the interferogram at any time instant as an input argument and performs filtering and optimization with wavelet detrending. As shown in Figure 8, the spectrum was normalized, and zero-crossing detection was performed. From this, FSR values are estimated which are used to calculate an approximate mean cavity length. The cavity length is inversely computed to obtain a singular FSR from which the interferogram is reconstructed. Zero-crossing detection was performed again on the reconstructed spectrum. This spectrum reconstruction eliminates the phase noise from the signal, yielding a constant FSR value from which accurate cavity length can be determined in real-time.

4. RESULTS AND DISCUSSIONS

Experiments were performed by pouring the molten flux into the instrumented mold at a temperature of 1400 ºC. The point gap sensors installed in the mold measured the air gap between mold wall and shrinking flux as well as flux thickness due to the formation of an extrinsic EFPI. The formation of multiple reflectors in the EFPI as shown in Figure 6, which gives a modulated interferogram that is captured by the EFPI sensors dynamically as the flux undergoes solidification. After the mold flux solidifies completely, a stable modulated interferogram was observed, which suggests that the flux film’s air gap and thickness reaches steady state fairly rapidly. The solidified flux sample is shown in Figure 9, from which it can be observed that the flux sample is translucent. The coloring of flux film sample after solidification is dependent on its basicity and composition [36,37].

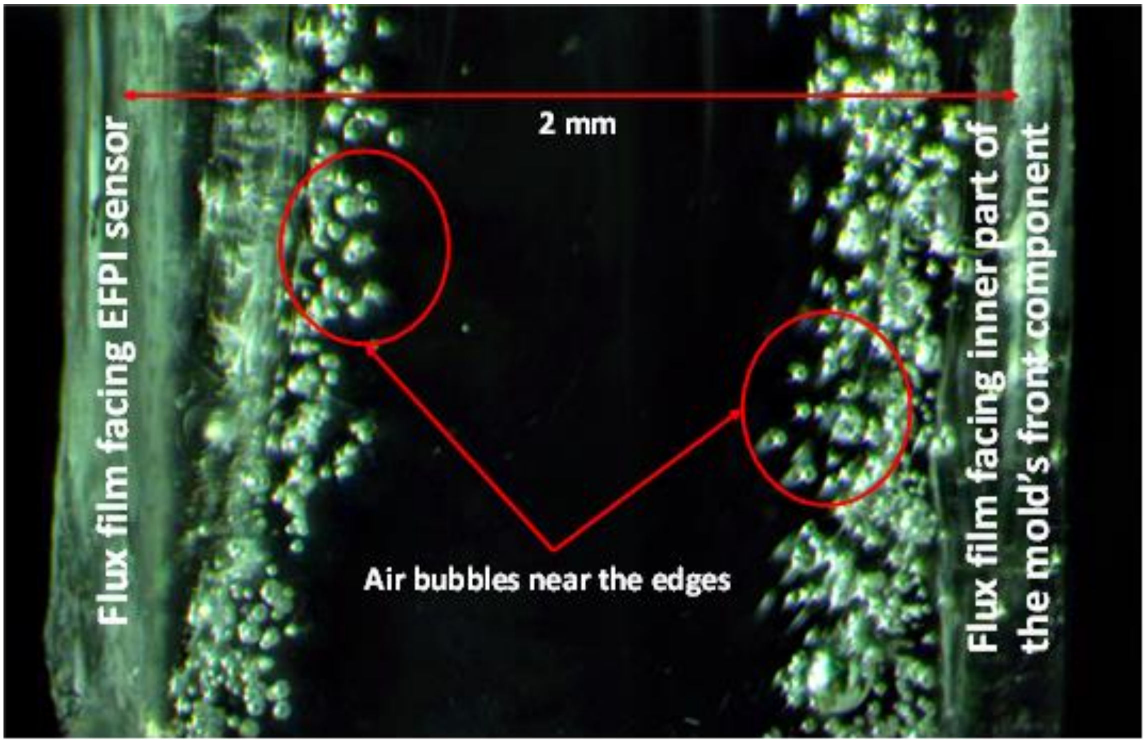

Figure 9. H2-9 flux sample after solidification. It is translucent in appearance due to the overall composition. The flux basicity can influence the amount of bubble formation in the flux. During solidification, it can be observed that the air bubbles get trapped within the flux near the edges which result in the interferogram modulation.

4.1. INTERFEROGRAM

Interferograms acquired from the 3 EFPIs installed in the mold are shown in Figure 10 for both the trials. Each mold step where the mold flux solidifies has a different reflectivity. This is the reason for the changing fringe visibility in each step of the mold.

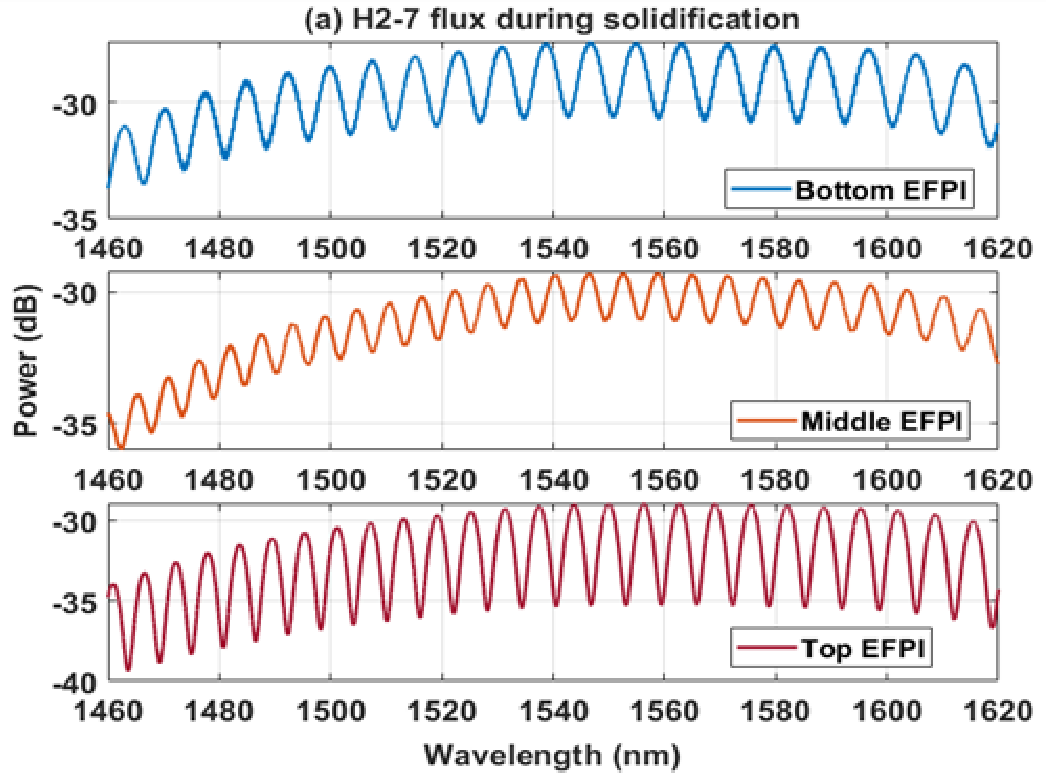

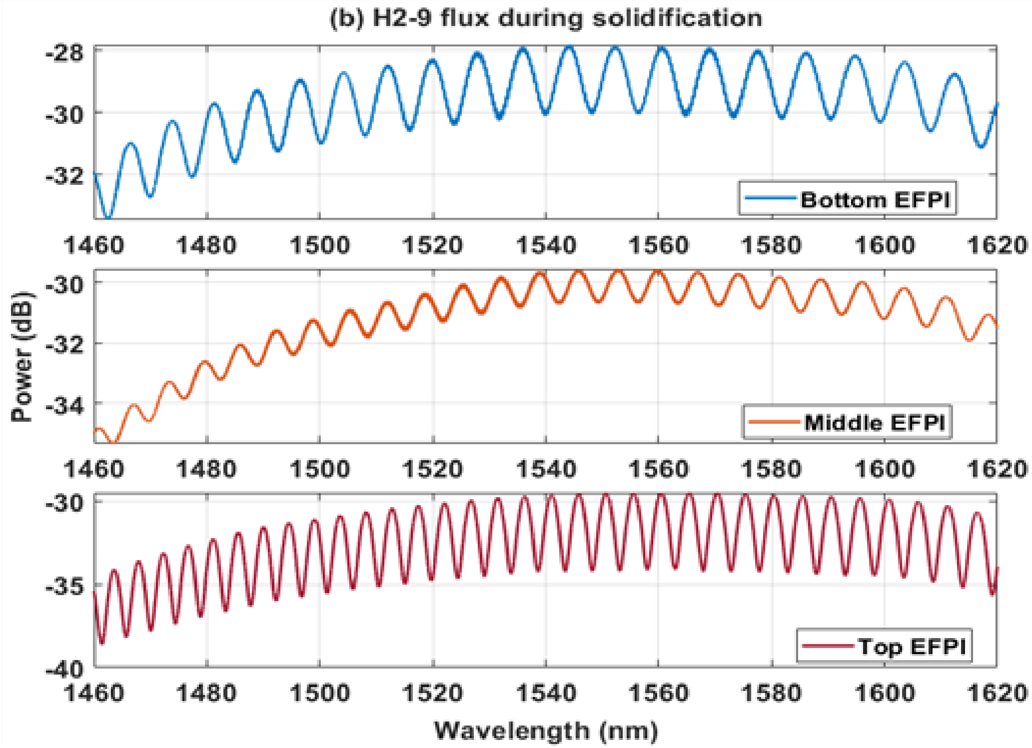

Figure 10. Interferogram for solidification of mold flux samples. a) H2-7 flux and b) H2-9 flux. Spectra shown here are after 2 mins of the pour for each experimental trial. The measured spectra are modulated indicating multiple reflectors being formed in the flux.

Interferograms from each mold flux experiment are presented only for the bottom EFPI, as the optical interrogator's maximum measurement range is limited to 3.5 mm, which is exceeded by middle (4 mm) and top (6 mm) step EFPI sensors in the mold.

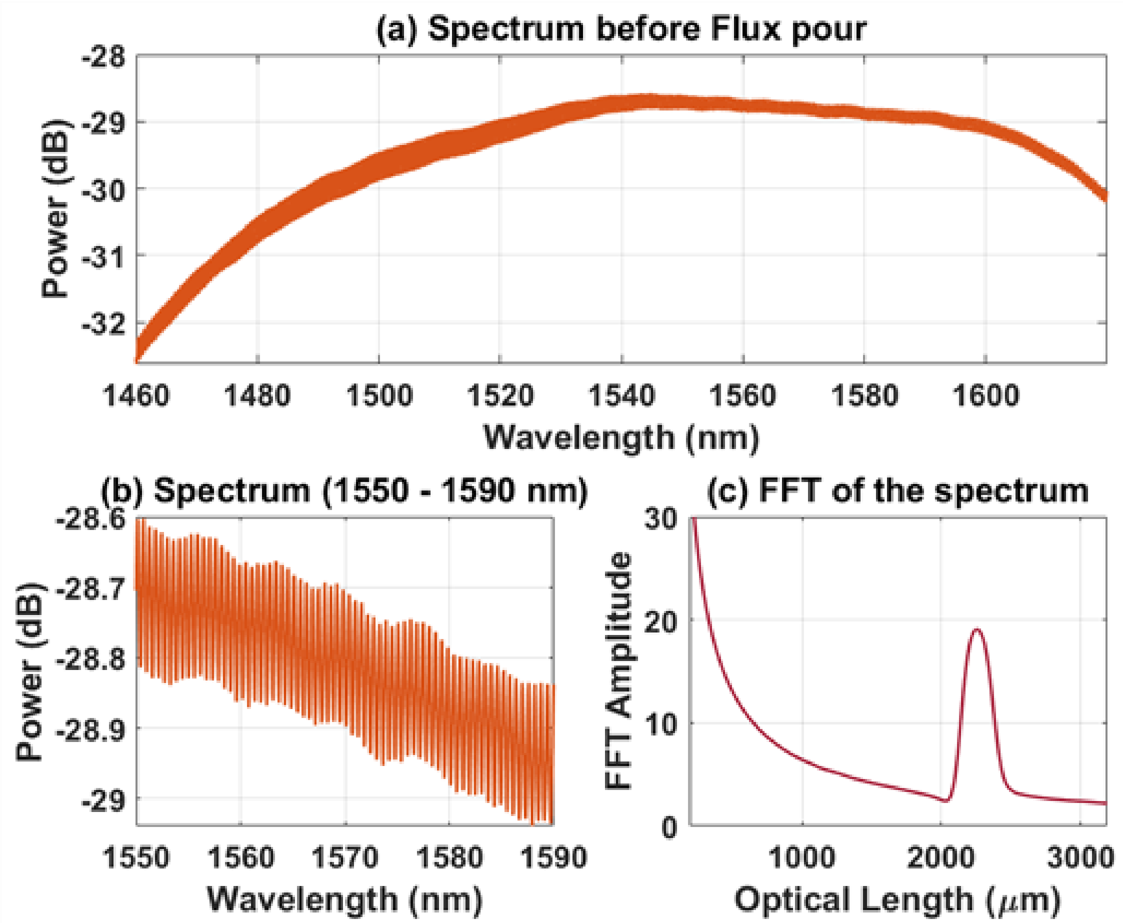

Figure 11. Bottom EFPI spectrum before the molten flux was poured into the mold. a) full spectrum of the mold gap acquired by the bottom EFPI before beginning the experiment. b) bottom EFPI spectrum before experiment between 1550 nm and 1590 nm. c) Fast Fourier transform of the spectrum in (a), between 0 to 3500 µm.

The changes observed in the measured spectra for the bottom EFPI during flux solidification and shrinkage will now be discussed.

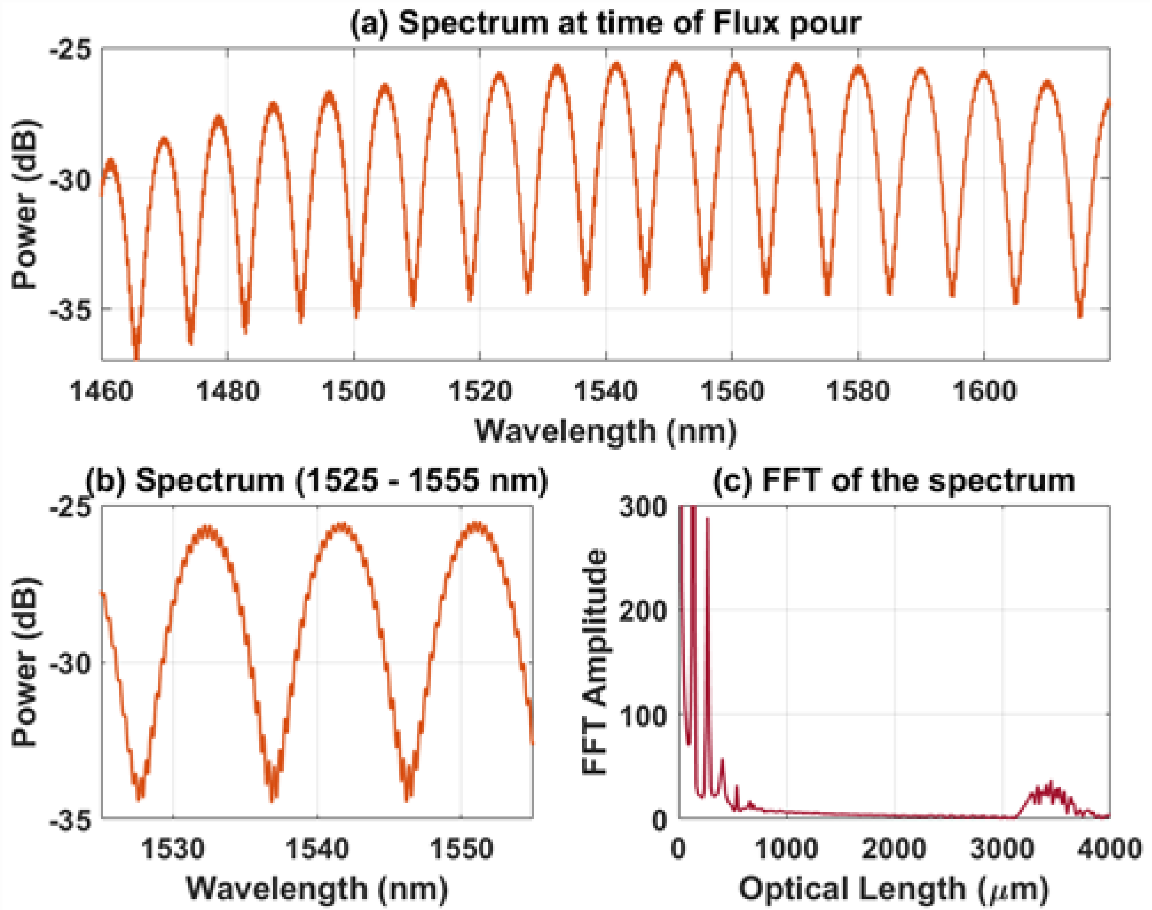

Figure 12. Bottom EFPI spectrum at the instance when molten flux was poured into the mold. a) full spectrum of the mold gap with flux sample acquired by the bottom EFPI at the instant of pouring. b) bottom EFPI spectrum at the instant of pour between 1525 nm and 1555 nm. c) Fast Fourier transform of the spectrum in (a), between 0 to 4000 µm.

Before flux was poured into the mold gap, the interferogram shown in Figure 11a was acquired. The parabolic trend of the interferogram is due to the signature of the swept laser from Hyperion SI-255 optical interrogator. The modulation of tis spectrum is shown in Figure 11b for the reflection of light from the interior of the opposite wall of the mold. This interferogram yields a total mold gap measurement of ~2 mm for the bottom EFPI sensor. The FFT of this spectrum with respect to optical length in µm is shown in Figure 11c, which shows a peak after the DC component at 2130 µm. This matches with the physical length of the mold gap. When the flux sample is poured into the mold, the acquired spectrum is as shown in Figure 12a. This is due to the mold gap getting filled with the molten flux. However, the EFPI demodulation algorithm with its advanced signal processing capability, estimates the air gap accurately. The FFT result for this spectrum is shown in Figure 12c. From this, it is observed that the air gap forms almost instantly. The short peak at 106.89 µm in the FFT signal corresponds to the air gap, which is formed due to rapid pull away of the flux film from mold wall. The peak at 2130 µm observed in Figure 11c, moves away to ~3300 µm and becomes broader as shown in Figure 12c. This is the optical path change due to the change in refractive index from air (~1) to flux (~1.52). The peak is broad because of the reflections from multiple air bubbles within the flux near the edge of solidified flux.

The interferogram acquired 4 seconds after pouring the molten flux sample into the mold is shown in Figure 13a. The peak and valley regions of this spectrum appear to be thicker. From this, it can be inferred that the signal is modulated. This means that there are multiple reflectors being formed within the flux material. This is evident by observing the signal between 1570 nm and 1600 nm as shown in Figure 13b. The interferogram was processed to obtain FFT as shown in Figure 13c. Multiple peaks were observed in this FFT signal.

The large peak at the right side of DC component corresponds to total air gap between mold wall and mold flux sample undergoing solidification. Smaller peaks neighboring air gap peak corresponds to the reflection from the trapped air bubble at ~400 µm being formed within the flux material. The FFT signal between 3000 µm and 4000 µm consists of multiple peaks. The last peak towards the right side corresponds to the reflection from the interior of front component of mold wall and the remaining peaks are due to reflections from trapped air bubbles within the flux close to the edge.

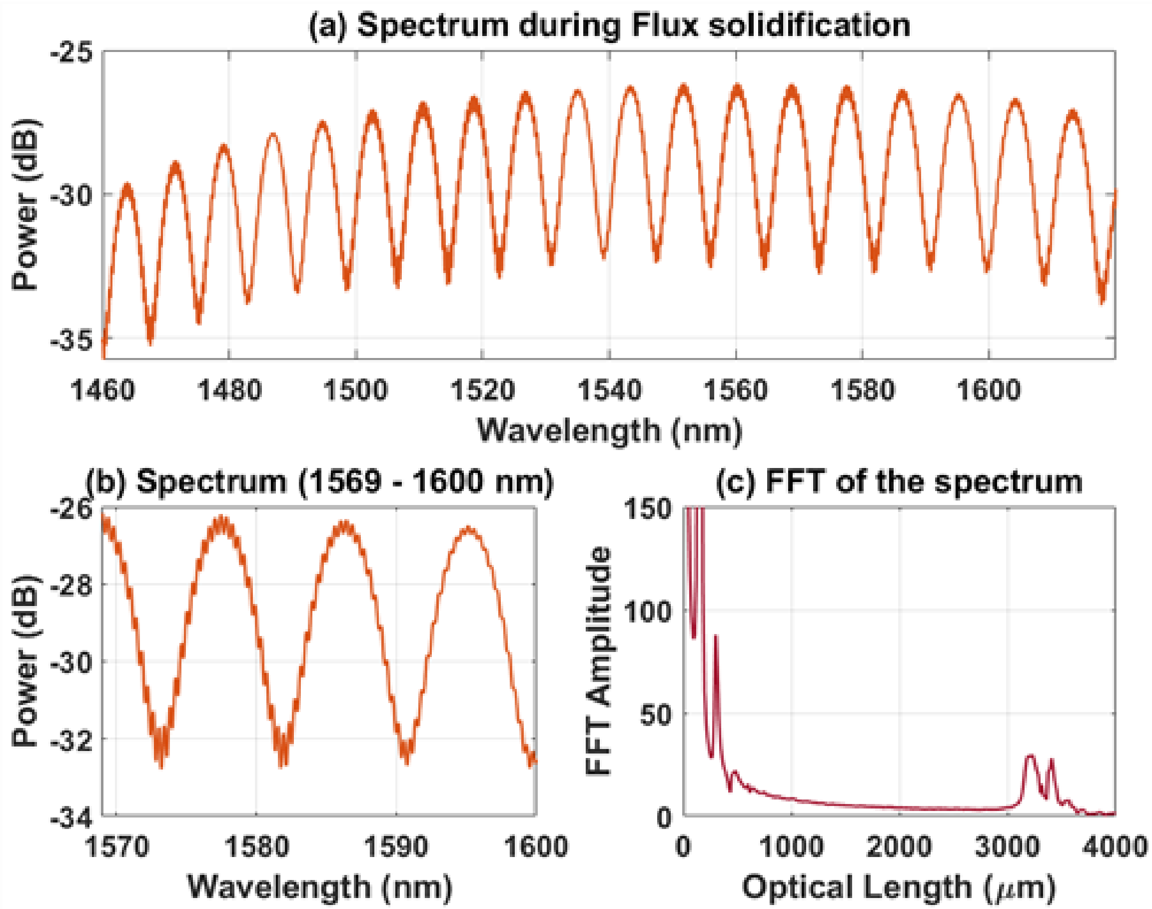

Figure 13. Bottom EFPI spectrum acquired 4 seconds after molten flux was poured into the mold. a) full spectrum of the mold gap with flux sample acquired by the bottom EFPI 4 seconds after pouring the sample. b) bottom EFPI spectrum after 4 seconds of pour between 1570 nm and 1600 nm. c) Fast Fourier transform of the spectrum in (a), between 0 to 4000 µm.

Each flux material composition in (wt. %) ratio is given in this table along with basicity information in Table 2. To get modified basicity of H2-7, aluminum oxide content was varied and balanced with silica. For H2-9, silica was varied and balanced with calcium oxide maintaining constant aluminum oxide content. Molten flux samples are relatively viscous (0.5 – 0.4 Poise), which makes filling difficult in small gaps such as 2 mm.

Viscosity of flux sample is reduced by increasing the basicity of the material. Basicity and composition of flux samples used in this experiment are included in Table 2. The information in the table is in percentage weight ratio.

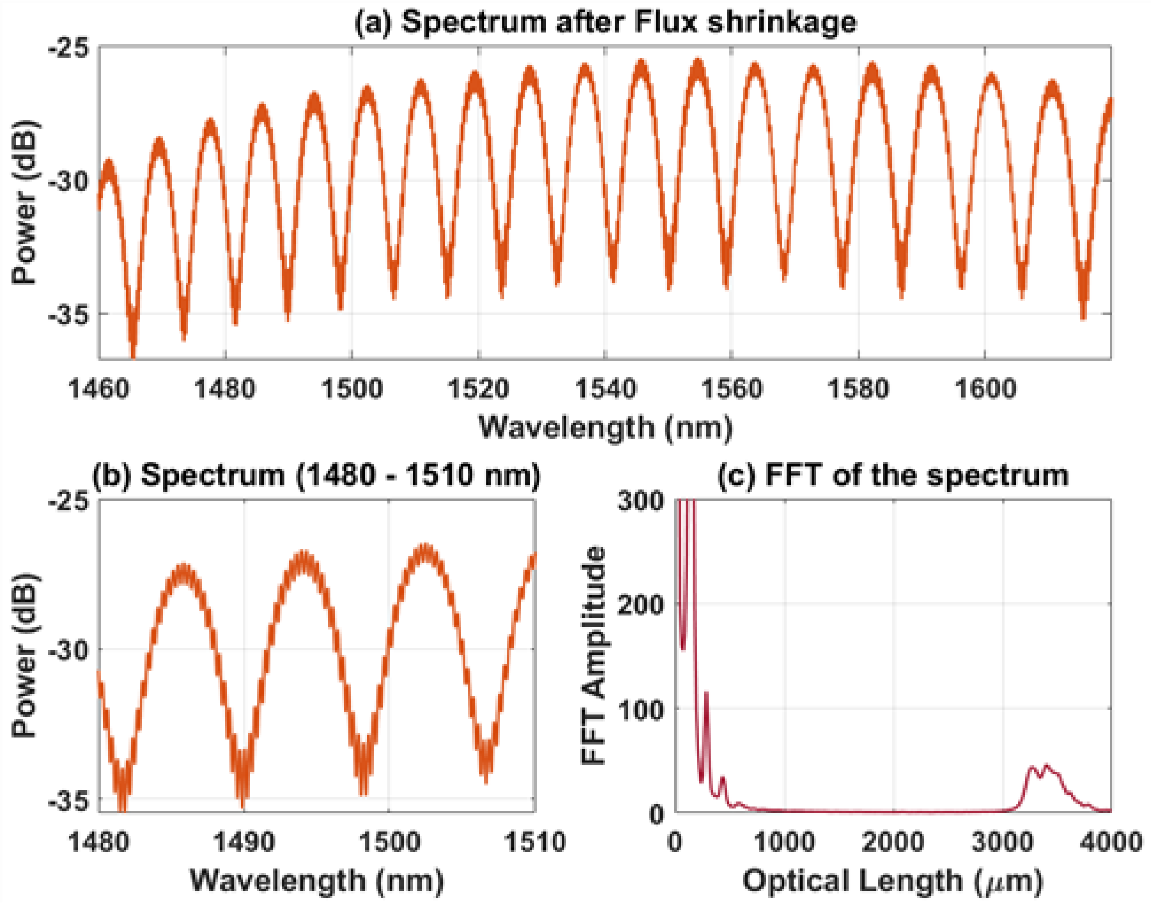

Figure 14. The bottom EFPI spectrum acquired after solidification of molten mold flux in the mold. a) full spectrum of the mold gap with solidified flux sample inside, acquired by the bottom EFPI. b) bottom EFPI spectrum between 1480 nm and 1510 nm after solidification of molten flux. c) Fast Fourier transform of the spectrum in (a), between 0 to 4000 µm.

The interferogram shown in Figure 14a was acquired after the mold flux completely solidified. It appears thicker than the interferogram shown in Figure 13a. At this time, the flux film has cooled to the temperature of the mold and has undergone shrinkage. From the FFT of interferogram shown in Figure 14c, it can be observed that all the peaks after DC component have shifted slightly towards the right i.e., increase in optical length. The peaks have also increased in terms of reflected power because of the transparency of the flux sample. The peaks observed in the FFT for the acquired interferogram are used to determine the thickness and location of trapped air bubbles as discussed in the measurement theory section.

Table 2. Mold Flux Composition

Flux composition (wt. %)	***H2-7***	***H2-9***
CaO	0.29	0.30
SiO_2	0.27	0.29
MgO	0.04	0.04
Al_2O_3	0.13	0.10
Na_2O	0.15	0.15
F	0.09	0.09
Basicity	1.06	1.06

4.2. AIR GAP MEASUREMENT

The air gap measurement is obtained directly by processing the interferogram using the low finesse EFPI demodulation algorithm as it is a low frequency signal demodulation. It ignores the higher frequencies in the case where interferogram is modulated. That is, the developed algorithm is intelligent enough to recognize that the lowest frequency of the acquired interferogram is due to the manifestation of the air gap due to flux film shrinkage during the quenching process.

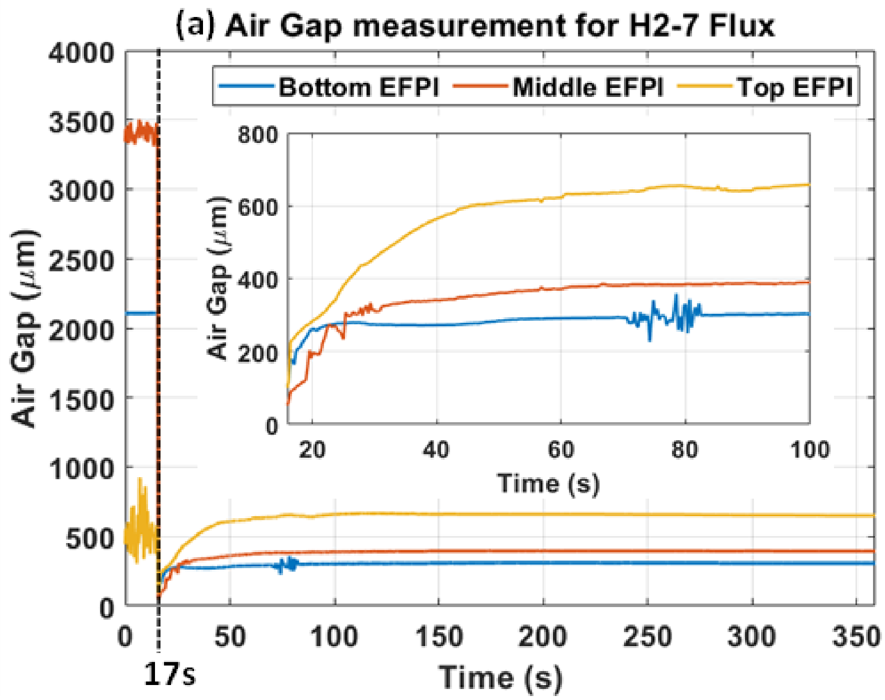

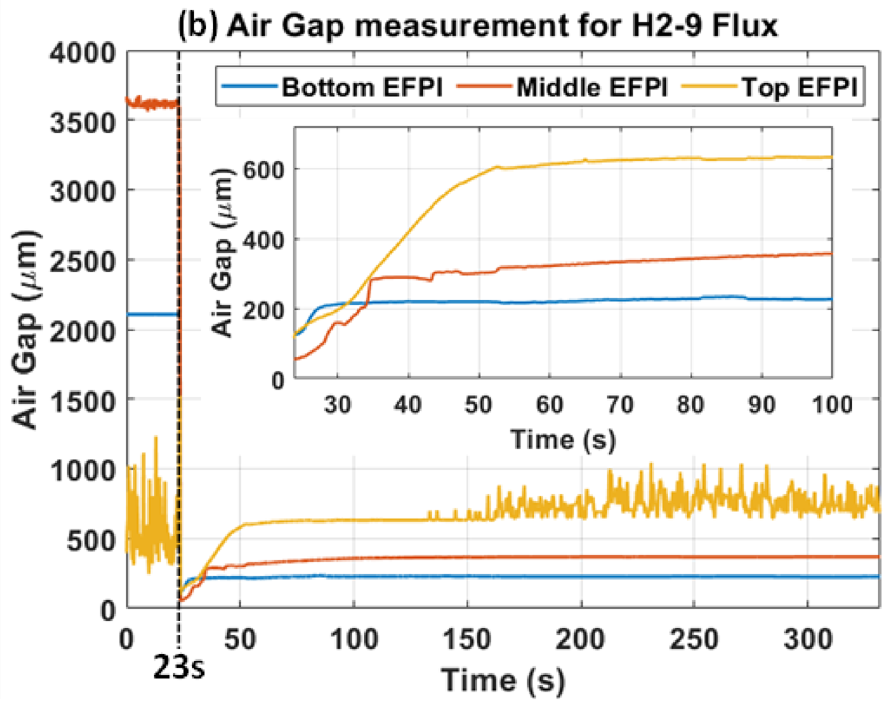

Figure 15. Air gap or cavity length estimated in real-time by the low finesse EFPI demodulation algorithm. a) H2-7 flux sample air gap, and b) H2-9 flux sample air gap. The figure inserts show the first 100 seconds of the air gap measurement which involves the solidification. Phenomena such as crack formation and propagation can be seen. Cracking is due to the release of internal stresses built up due to fast quenching of the molten mold flux.

Table 3. Air Gap After Flux Solidification

Air gap after solidification	***H2-7***	***H2-9***
Top EFPI (μm)	650.12	686.19
Middle EFPI (μm)	394.62	368.49
Bottom EFPI (μm)	306.93	226.59

The top and middle EFPI signal measurement is not very clear before the pour in each trial as the step profile's mold gap is 4 mm and 6 mm at these sensor locations. This is beyond the measurement capability of the optical interrogator. Hence, only the bottom EFPI shall be considered for the thickness estimation. The air gaps are calculated according to equation (2) in the measurement theory section. The air gap plots shown in Figure 15 have spikes at certain times, for example in Figure 15a between 70 to 80 seconds. This is due to the cracking of mold flux film inside the mold due to stresses that develop during rapid cooling of the flux film.

The air gap measurements gradually became stable after the molten flux started to solidify. Gap measurements ultimately reached the values shown in Table 3. At the time of pouring, the cavity lengths measured are approximately equal to the internal offsets shown in Table 1. As the flux samples solidify and shrink, the air gaps gradually reach the values shown here. When the mold flux basicity was high, slight temperature differences can induce the cracking which was observed in Figure 15b. The cracking phenomena of H2-9 flux was evident from 150 seconds of top EFPI's measurement. The cracks formed during solidification are shown in Figure 16. The crack formation and propagation can be minimized by pre-heating the mold before performing the experiment. This way the window of measurement can also be extended as the flux crystallization period is prolonged.

Figure 16. Cracking seen during solidification of H2-9 flux film sample. The solidifying flux sample vibrates during crack formation which leads to the noisy air gap measurement as shown in Figure 15. The effects of cracking can be minimized by pre-heating the mold before the experiment.

4.3. THICKNESS MEASUREMENT

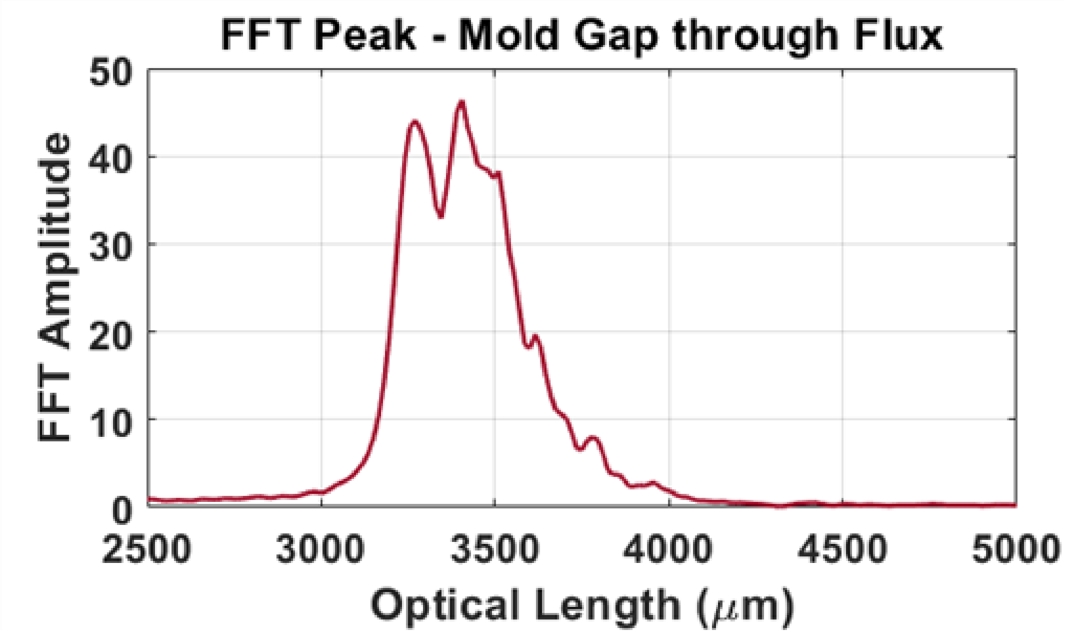

Figure 17. FFT peak from which spectrum is reconstructed for mold gap estimation through the flux medium. For each spectrum acquired from the EFPI sensor, the FFT signal is processed and the right most peak is detected. The spectrum is reconstructed, and the mold gap is determined using a low finesse EFPI demodulation algorithm in real-time. The mold gap thickness is corrected with the corresponding refractive index of flux.

The bottom EFPI acquired interferogram is processed to obtain FFT and the right most peak was selected for spectrum reconstruction as shown in Figure 17. Then, a low finesse EFPI demodulation algorithm was used to estimate the optical length of the mold gap through each flux medium. This optical length was corrected with the appropriate refractive index to obtain the exact mold gap length (~2 mm) as shown in Figure 18. At certain times, the optical length of the mold may exceed the machined mold cavity since the RI is being assumed as a constant of 1.52.

The thickness of the solidified mold flux film was measured by estimating the real-time difference between the air gap measurement by bottom EFPI shown in Figure 15 and the mold gap estimates shown in Figure 18 at each time instant of the experiment. These results were based on equation (8). The thickness measurements shown in Figure 19 matched the post experiment physical measurements.

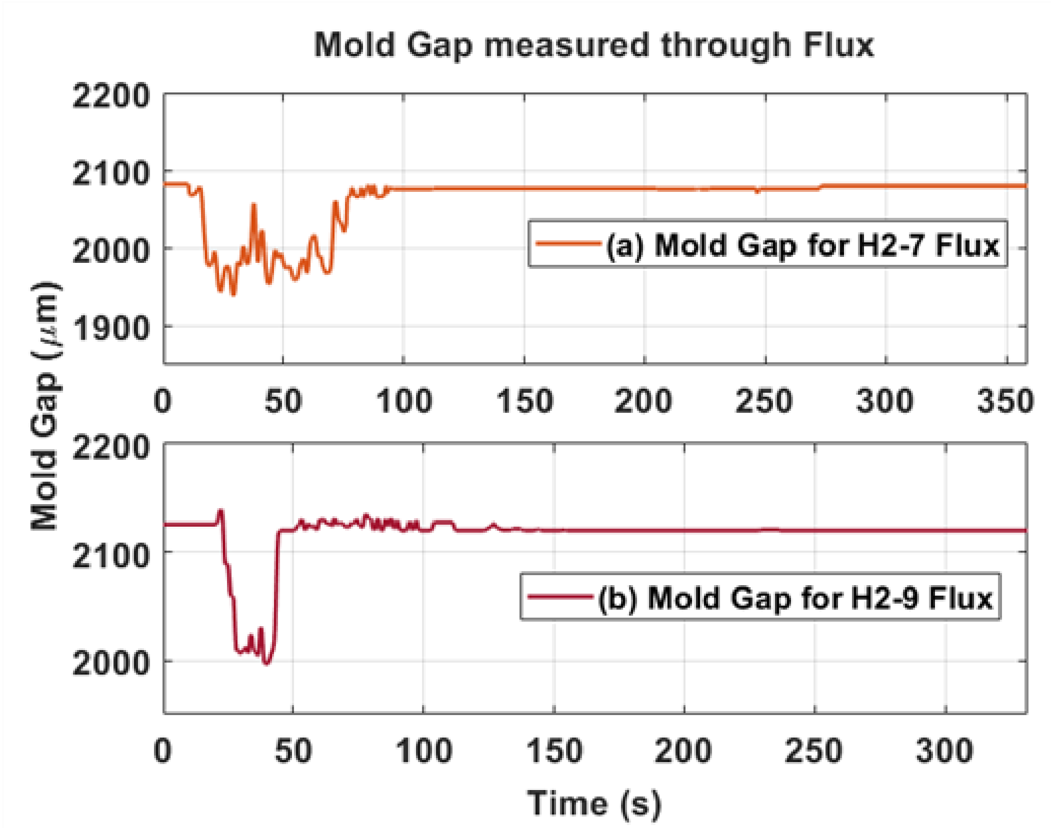

Figure 18. Mold gaps measured for each flux sample during solidification. (a) mold gap measured through H2-7 flux, where the measurement varies ~120 µm up to 80 seconds, after which it remains stable. (b) mold gap measured through H2-9 flux, where the measurement varies ~100 µm up to 50 seconds, after which the variations reduce to ~10 µm before becoming stable.

The thickness measurement indicates the total mold gap length (~2 mm) before the molten flux sample was poured into the mold. For the thickness measurement of H2-7 flux shown in Figure 19a, the flux thickness varies between 30 to 80 seconds due to the crack formation during the rapid quenching. The thickness measurement of H2-9 flux is shown in Figure 19b. It can be observed that thickness measurement reaches stability faster than H2-7 flux.

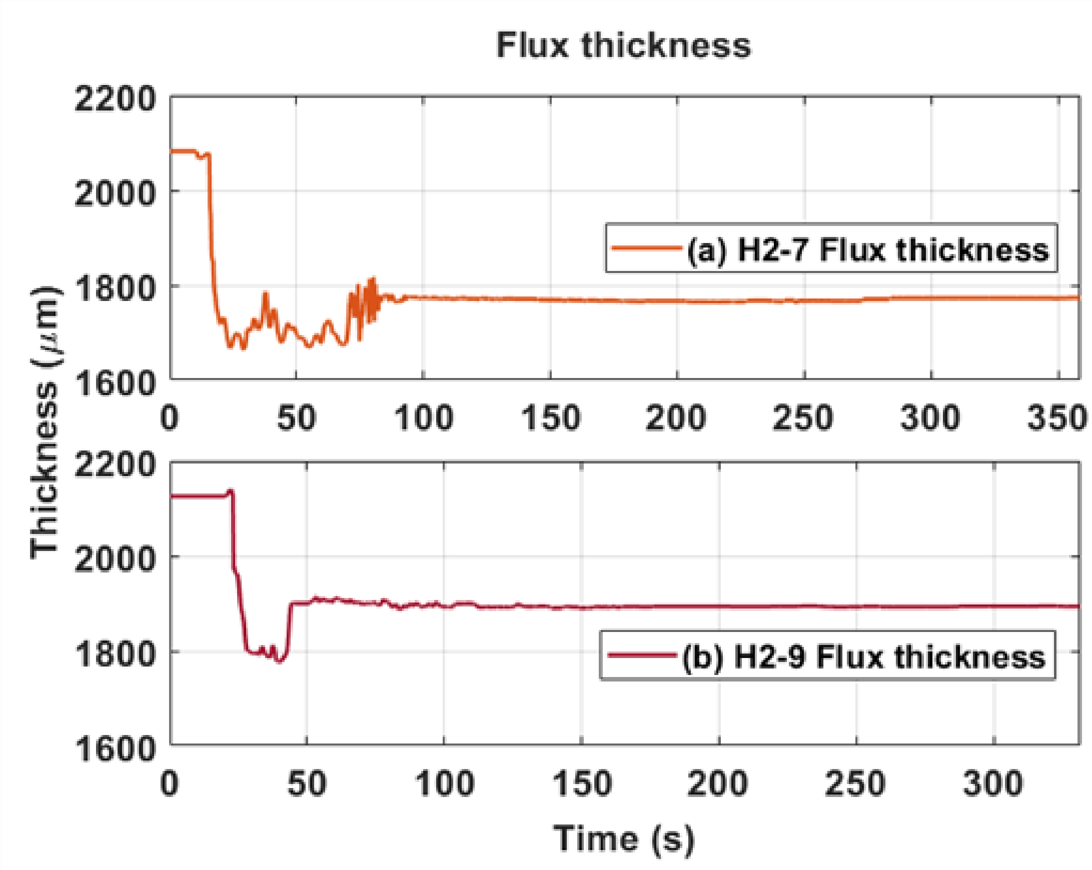

Figure 19. Real-time thickness measurement of mold flux. a) H2-7 real-time thickness, and c) H2-9 real-time thickness. The thickness is a difference between air gap and the mold gap divided by RI of 1.52. The flux thickness measurement remains consistently stable after 100 seconds in case of H2-7 flux and 50 seconds in case of H2-9 flux.

4.4. REFLECTION FROM AIR BUBBLES WITHIN THE FLUX

The proposed algorithm can also be used to locate the air bubbles being formed within the flux film sample. A few air bubbles get trapped and freeze directly in the path of the EFPI sensor directed light as shown in Figure 20.

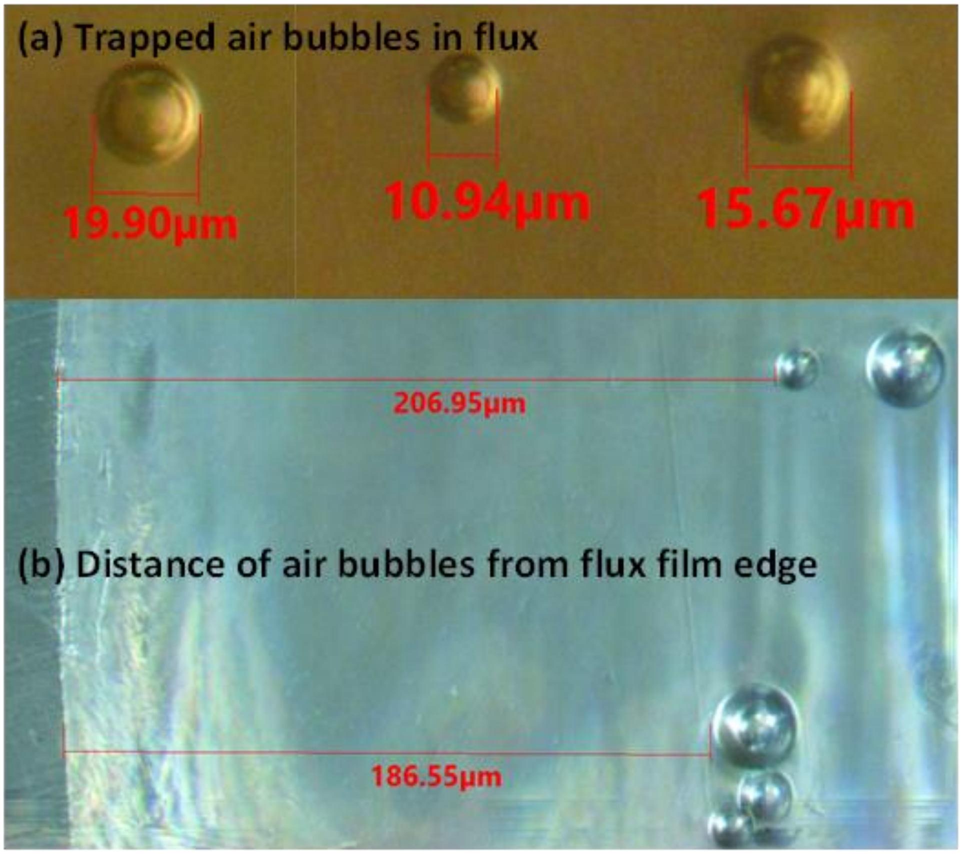

Figure 20. Flux sample with air bubbles in EFPI path. a) Trapped air bubbles in flux and b) Distance of sir bubbles from flux film edge facing EFPI sensor. After a portion of light gets reflected at the flux film’s edge in the air gap, some light penetrates the flux film boundary and goes though the flux, where again some light gets reflected by the trapped air bubble within the flux. The air bubbles shown here are at 206.95 µm and 186.55 µm from the flux film boundary.

Position with respect to time can be determined in real-time with the EFPI sensor or mold wall as the reference. Considering the FFT transform of the interferogram, the second peak in Figure 20 insert is detected and tracked using peak detection and the spectrum at this optical length is reconstructed. The low finesse EFPI demodulation algorithm is used to estimate the distance from this reconstructed spectrum. This allows for real-time monitoring of the air bubble location as shown in Figure 21. This estimation is in accordance with equation (10). This method can be extended to measure the distances of multiple air bubbles within the flux during the solidification process depending on the number of peaks in the FFT signal. The variations in measurement are higher when the flux sample is still in molten phase. However, as the flux sample solidifies, the air bubble gets trapped in place due to rapid quenching, resulting in a stable measurement.

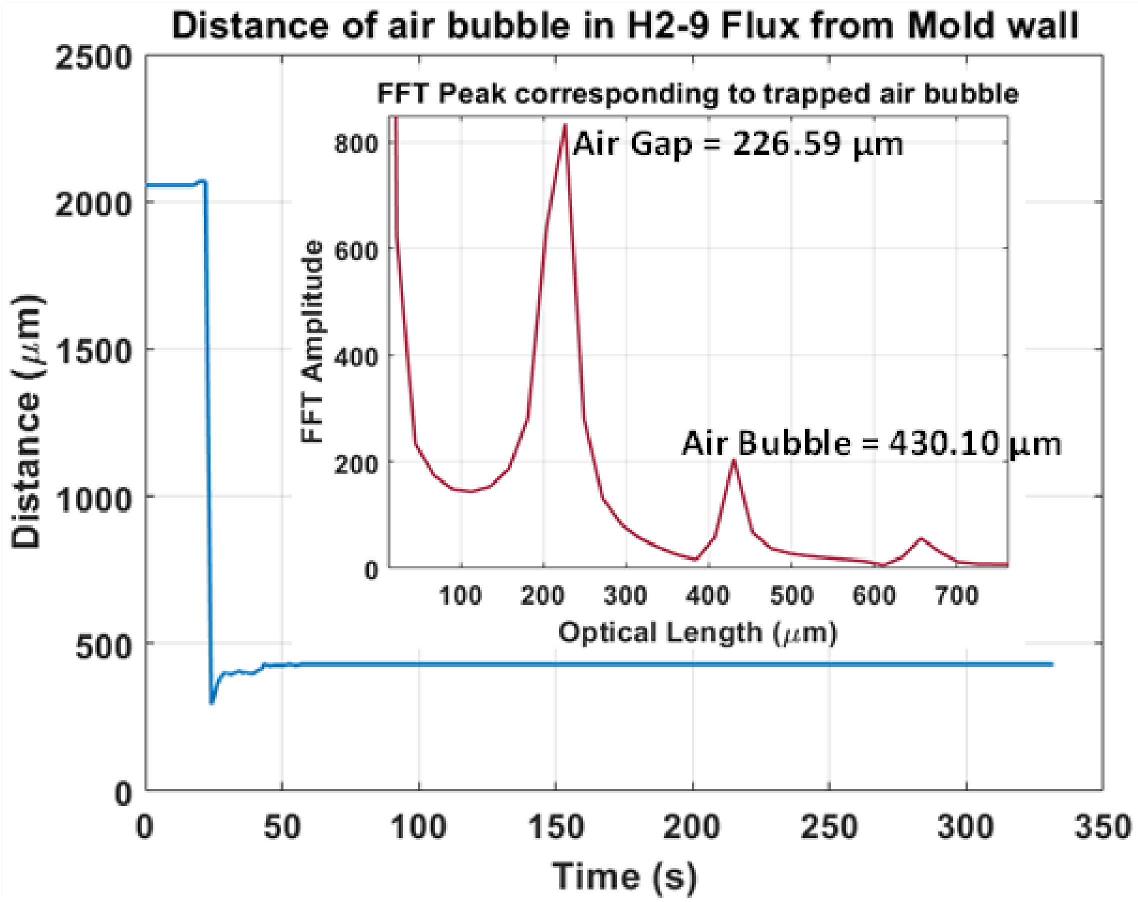

Figure 21. Real-time location of air bubble in H2-9 mold flux from the EFPI sensor. The figure insert depicts FFT of the interferogram during the solidification of H2-9 flux. Two distinct peaks can be observed, where the large peak corresponds to air gap and the small peak to its right corresponds to the reflection from the air bubble trapped within the flux.

The measurement shown in Figure 21 indicates an air bubble located at 430.10 µm from the EFPI sensor. This matches with the physical distance of the air bubble within flux film from the EFPI sensor, shown in Figure 20. For H2-9 flux sample, the air gap after flux shrinkage is 226.59 µm and the air bubble is located at 206.95 µm from the flux film boundary. On adding these two values, one can obtain 433.54 µm, which is very close to the measured distance in Figure 21.

5. CONCLUSION

In this research, a 3-part stainless-steel mold with a three-step profile was designed and constructed and then successfully used for air gap and thickness measurements. Three EFPIs were instrumented successfully and installed in the center of each step profile of the mold such that they were in flush with the mold wall. Mold flux samples were melted in a furnace and poured into the mold setup. The real-time interferogram was successfully acquired using a Hyperion SI255 optical interrogator. A low finesse EFPI demodulation algorithm was developed to measure the air gap and thickness from the modulated interferogram in real-time. Information regarding the presence of trapped air bubbles within the mold flux film was obtained from the modulated interferogram in real-time. The proposed system of measurement can be applied in real-time monitoring of the shrinkage of molten metals as well. Several EFPIs in an array can be used to obtain high resolution information regarding the surface properties of the materials at high temperatures.

ACKNOWLEDGEMENT

The views and opinions of authors expressed herein do not necessarily state or reflect those of the United States Government or any agency thereof. This research was funded by Subaward Number SPI016 under United States Government Prime Agreement Number SP4701-20-C-0076, the U.S. Department of Energy’s Office of Energy Efficiency and Renewable Energy (EERE) under the Advanced Manufacturing Office (AMO) Award

DE-EE0009119, and the Peaslee Steel Manufacturing Research Center (PSMRC) at the Missouri University of Science and Technology Rolla MO, USA. (Corresponding author: Jie Huang, jieh@mst.edu). Abhishek Prakash Hungund and Hanok Tekle contribute equally to this work.

Abhishek Prakash Hungund, Bohong Zhang, Rex E. Gerald II, and Jie Huang are with Department of Electrical and Computer Engineering, Missouri University of Science and Technology, Rolla, MO 65409 USA (e-mail: jieh@mst.edu).

Hanok Tekle, Ronald J. O’Malley, Jeffrey D. Smith, and Todd Sander are with Department of Materials and Science Engineering, Missouri University of Science and Technology, Rolla, Missouri, 65409 (e-mail: omalleyr@mst.edu). Special thanks Zoey Snyder from Material science department for assistance in polishing the flux film.

REFERENCES

[1] Mills, K. C., and A. B. Fox. "Mould fluxes." High Temperature Materials and Processes 22.5-6 (2003): 291-302.

[2] Wang, Xufeng, et al. "Effect of AlN on properties of non-reactive CaO-Al2O3-based mold flux for high-Al steel." Materials Today Communications (2023): 105432.

[3] Yamauchi, Akira, et al. "Heat transfer between mold and strand through mold flux film in continuous casting of steel." ISIJ international 33.1 (1993): 140-147.

[4] Deng, Xiaoxuan, et al. "Inclusion behaviour in aluminium-killed steel during continuous casting." Ironmaking & Steelmaking 46.6 (2019): 522-528.

[5] Pinheiro, C. A. M., et al. "Mould heat transfer and continuously cast billet quality with mould flux lubrication Part 1 Mould heat transfer." Ironmaking & Steelmaking 27.1 (2000): 37-54.

[6] Cramb, A.W., The Making, Shaping and Treating of Steel: Casting Volume, ed. A.W. Cramb. 2003: AISE Steel Foundation.

[7] Peterson, Elizabeth Irene, "Mold flux crystallization and mold thermal behavior" (2017). Masters Theses. 7656. https://scholarsmine.mst.edu/masters_theses/7656

[8] Headley, T. J., and R. E. Loehman. "Crystallization of a glass-ceramic by epitaxial growth." Journal of the American Ceramic Society 67.9 (1984): 620-625.

[9] Serbena, F. C., et al. "Crystallization toughening of a model glass-ceramic." Acta Materialia 86 (2015): 216-228.

[10] Beall, G. H. "Design and properties of glass-ceramics." Annual Review of Materials Science 22.1 (1992): 91-119.

[11] Wang, Xiaoyang, et al. "Flux growth of large KBBF crystals by localized spontaneous nucleation." Journal of crystal growth 318.1 (2011): 610-612.

[12] Baek, Ji-Yeon, et al. "Glass structure and crystallization via two distinct thermal histories: Melt crystallization and glass crystallization." Journal of the European Ceramic Society 41.1 (2021): 831-837.

[13] Cho, Jung Wook, and Hiroyuki Shibata. "Effect of solidification of mold fluxes on the heat transfer in casting mold." Journal of Non-crystalline solids 282.1 (2001): 110-117.

[14] Pan, Ting, et al. "Thermal shrinkage behavior of metal–organic frameworks." Advanced Functional Materials 30.34 (2020): 2001389.

[15] Brennan, M. C., J. S. Keist, and T. A. Palmer. "Defects in metal additive manufacturing processes." Journal of Materials Engineering and Performance 30.7 (2021): 4808-4818.

[16] Yamauchi, Akira, Toshihiko Emi, and Seshadri Seetharaman. "A mathematical model for prediction of thickness of mould flux film in continuous casting mould." ISIJ international 42.10 (2002): 1084-1093.

[17] Yi, Kyung-Woo, Young-Tae Kim, and Dong-Yong Kim. "A numerical simulation of the thickness of molten mold flux film in continuous casting." Metals and Materials International 13.3 (2007): 223-227.

[18] J. E. Shelby. Introduction to glass science and technology. Second Edition. Cambridge Royal Society of Chemistry, 2005.

[19] Vorathin, E., et al. "Review of high sensitivity fibre-optic pressure sensors for low pressure sensing." Optics & Laser Technology 121 (2020): 105841.

[20] Ahsani, Vahid, et al. "Tapered fiber-optic Mach-Zehnder interferometer for ultra-high sensitivity measurement of refractive index." Sensors 19.7 (2019): 1652.

[21] Rodriguez-Schwendtner, Eva, et al. "Advanced plasmonic fiber-optic sensor for high sensitivity measurement of magnetic field." IEEE Sensors Journal 19.17 (2019): 7355-7364.

[22] Zhu, Chen, et al. "A miniaturized optical fiber tip high-temperature sensor based on concave-shaped Fabry–Perot cavity." IEEE Photonics Technology Letters 31.1 (2018): 35-38.

[23] Minakuchi, Shu, et al. "Thermal strain in lightweight composite fiber-optic gyroscope for space application." Journal of Lightwave Technology 33.12 (2014): 2658-2662.

[24] Stiles, Claire M., Quentin R. Stiles, and Judson S. Denson. "A flexible fiber optic laryngoscope." Jama 221.11 (1972): 1246-1247.

[25] Shao, Li-Yang, and Jacques Albert. "Compact fiber-optic vector inclinometer." Optics letters 35.7 (2010): 1034-1036.

[26] Garcus, D., et al. "Brillouin optical-fiber frequency-domain analysis for distributed temperature and strain measurements." Journal of lightwave technology 15.4 (1997): 654-662.

[27] Ukil, Abhisek, Hubert Braendle, and Peter Krippner. "Distributed temperature sensing: Review of technology and applications." IEEE Sensors Journal 12.5 (2011): 885-892.

[28] Zhu, Chen, et al. "A displacement sensor with centimeter dynamic range and submicrometer resolution based on an optical interferometer." IEEE Sensors Journal 17.17 (2017): 5523-5528.

[29] Chen, Haibin, et al. "Fiber-optic, extrinsic Fabry–Perot interferometric dual-cavity sensor interrogated by a dual-segment, low-coherence Fizeau interferometer for simultaneous measurements of pressure and temperature." Optics Express 27.26 (2019): 38744-38758.

[30] Ahn, Soyeon, et al. "Fiber-optic Temperature Sensor based on Cholesteric Liquid Crystals using 1250 nm band,> 220 nm Wideband Wavelength-swept Laser." Optical Fiber Sensors. Optica Publishing Group, 2022.

[31] Lee, Gi Hyen, et al. "Output Characterization of 220 nm Broadband 1250 nm Wavelength-Swept Laser for Dynamic Optical Fiber Sensors." Sensors 22.22 (2022): 8867.

[32] Yamashita, Shinji, et al. "Wide and fast wavelength-swept fiber laser based on dispersion tuning for dynamic sensing." Journal of Sensors 2009 (2009).

[33] M. Njegovec and D. Donlagic, "Interrogation of FBGs and FBGs Arrays Using Standard Telecom DFB Diode," in Journal of Lightwave Technology, vol. 34, no. 22, pp. 5340-5348, 15 Nov.15, 2016, doi: 10.1109/JLT.2016.2616725.

[34] Ni, Wenjun, et al. "Ultrathin graphene diaphragm-based extrinsic Fabry-Perot interferometer for ultra-wideband fiber optic acoustic sensing." Optics express 26.16 (2018): 20758-20767.

[35] Ran, Zengling, et al. "A miniature fiber-optic refractive-index sensor based on laser-machined Fabry–Perot interferometer tip." Journal of Lightwave Technology 27.23 (2009): 5426-5429.

[36] Zhang, Bohong, et al. "In Situ and Real-Time Mold Flux Analysis Using a High-Temperature Fiber-Optic Raman Sensor for Steel Manufacturing Applications." Journal of Lightwave Technology (2023).

[37] Zhang, Bohong, et al. "In Situ High-Temperature Raman Spectroscopy via a Remote Fiber-Optic Raman Probe." IEEE Transactions on Instrumentation and Measurement (2023).

SECTION

3. CONCLUSIONS AND RECOMMENDATIONS

3.1. CONCLUSIONS

The main objective of this work is to perform real-time measurement or determination of the mold flux air gap and thickness during shrinkage due to cool down, which is a consequence of mold flux crystallization and solidification. To this end, a fiber optic based extrinsic Fabry-Perot Interferometer (EFPI) is designed in-house to perform real-time measurement.

In Paper I, a novel EFPI sensor having simple and robust design with high sensitivity for real-time air gap and thickness measurements is reported. The designed sensor can be configured as a distance measuring optical probe for high temperature applications and has good scope in the continuous casting industry.

The mathematical principle of a fiber optic EFPI is reported, proving the theoretical capacity to measure dynamic changes in the optical path length of the EFPI. The sensitivity is improved, and measurement variations are made much finer with the new advanced signal processing based low finesse EFPI demodulation algorithm to achieve a high resolution of 5-8 nm with a range of 10-1000 µm and 0.1-0.3 µm with a range of 1-3.5 mm.

To validate the EFPI sensor performance, high temperature continuous caster mold flux is targeted. Mold flux is used to cover the surface of the melt meniscus and fill the gap between the mold and the solidifying shell during the continuous casting process. The air gap is the space between the solidifying shell and the mold. By measuring the thickness of the mold flux film and air gap, the distribution behaviors and their effects on heat transfer and lubrication are analyzed. This leads to optimization of the casting process and mold structure. It has been observed that the lower melting temperature of mold flux results in greater liquid slag thicknesses, and conversely, the maximum air gap thicknesses decrease. Existing ranges also get smaller, which is more favorable for the strand lubrication. Furthermore, viscosity and fluidity of mold flux have a decisive influence on the infiltration of liquid slag in the mold gap, which affects the lubrication between the steel and the mold. The thickness of the air gap affects the degree of superheating of incoming molten metal, where the incoming molten metal is at a higher temperature than its melting point. The degree of superheating also affects the formation and thickness of the air gap and presents a viable alternative for control of the system.

In summary, measuring mold flux air gap and thickness can help in understanding the distribution behaviors, the effect on heat transfer, lubrication, and superheating, and provides insight into the optimization of the casting process and mold structure, which ultimately improves the quality of steel in continuous casting.

3.2. RECOMMENDATIONS FOR FUTURE WORK

Measuring mold flux air gap and thickness is crucial for ensuring the quality of steel in continuous casting. The ability to perform real-time measurement of these parameters can significantly improve the quality of manufactured steel while reducing the cost of production. The mold in continuous casting is exposed to high heat flux due to its contact with the hot molten metal, and the state of heat transfer in the mold and steel solidification depend on the magnitude of the mold boundary heat flux. Therefore, real-time measurement of the mold flux air gap and thickness can aid in optimizing the casting process and mold structure, leading to improved heat transfer and lubrication between the mold and steel.

Real-time measurement of the shrinkage of a molten steel strand being cast into a steel slab caster will be carried out as part of the continuation of this work. Continuous casting industry plant trials shall be conducted to validate the methodology of mapping the surface of the steel strand as it cools down from high temperature of ~1500 ºC from the mold. This is to aid in accelerating the industrialization of the EFPI gap measuring sensors, which can enable real-time monitoring of the steel shrinkage during the casting process.

The EFPI sensor setup shall be modified to accommodate an array of sensors, which can aid in mapping the surface of the steel strand as it cools down and solidifies, providing accurate measurements of the shrinkage rate. This information can be used to control the casting process, optimize the mold structure, and improve the quality of the manufactured steel. By reducing the occurrence of defects such as cracks, pores, and inclusions in the cast steel, the use of real-time measurement of mold flux air gap and thickness can lead to a higher yield of high-quality steel.

Real-time measurement of mold flux air gap and thickness, along with the future work on measuring the shrinkage of a molten steel strand being cast into a steel slab caster, can greatly impact the continuous casting industry by improving the quality of manufactured steel and reducing the cost of production. With the aid of modified EFPI gap measuring sensors, this technology can revolutionize the steel industry, making it more efficient and environmentally friendly.

BIBLIOGRAPHY

[1] Won, Young Mok, et al. "A new criterion for internal crack formation in continuously cast steels." Metallurgical and Materials Transactions B 31 (2000): 779-794.

[2] Monroe, R. "Porosity in castings." AFS Transactions 113 (2005): 519-546.

[3] Liu, Zhongqiu, Baokuan Li, and Maofa Jiang. "Transient asymmetric flow and bubble transport inside a slab continuous-casting mold." Metallurgical and Materials Transactions B 45 (2014): 675-697.

[4] Zhang, Zuotai, et al. "The influence of Al2O3/SiO2 ratio on the viscosity of mold fluxes." ISIJ international 48.6 (2008): 739-746.

[5] Cui, Heng, et al. "Formation of surface depression during continuous casting of high-Al TRIP steel." Metals 9.2 (2019): 204.

[6] Saraswat, Rajil, et al. "The effect of mould flux properties on thermo-mechanical behaviour during billet continuous casting." ISIJ international 47.1 (2007): 95-104.

[7] Lee, Dongwook, et al. "Defect detection algorithm in steel billets using morphological top-hat filter." IFAC Proceedings Volumes 42.23 (2009): 209-212.

[8] Baillie, Iain, et al. "Implementing an ultrasonic inspection system to find surface and internal defects in hot, moving steel using EMATs." Insight-Non-Destructive Testing and Condition Monitoring 49.2 (2007): 87-92.

[9] Edwards, R. S., et al. "EMAT and Eddy Current Dual Probe for Detecting Surface and Near-Surface Defects." AIP Conference Proceedings. Vol. 820. No. 1. American Institute of Physics, 2006.

[10] Jeon, Yong-Ju, et al. "Defect detection for corner cracks in steel billets using a wavelet reconstruction method." JOSA A 31.2 (2014): 227-237.

[11] Mehta, Bharat. "Surface and subsurface crack analysis in carbon steel samples using magnetic particle testing and liquid penetrant testing." Materials Evaluation 73.4 (2015).

[12] Kennedy, J. L., and N. Djeu. "Operation of Yb: YAG fiber-optic temperature sensor up to 1600 C." Sensors and Actuators A: Physical 100.2-3 (2002): 187-191.

[13] Fields, J. N., et al. "Fiber optic pressure sensor." The Journal of the Acoustical Society of America 67.3 (1980): 816-818.

[14] Zhao, Yang, and Farhad Ansari. "Quasi-distributed fiber-optic strain sensor: principle and experiment." Applied Optics 40.19 (2001): 3176-3181.

[15] Pospíšilová, Marie, Gabriela Kuncová, and Josef Trögl. "Fiber-optic chemical sensors and fiber-optic bio-sensors." Sensors 15.10 (2015): 25208-25259.

[16] Takeda, Nobuo. "Fiber optic sensor-based SHM technologies for aerospace applications in Japan." Smart Sensor Phenomena, Technology, Networks, and Systems 2008. Vol. 6933. SPIE, 2008.

[17] Yao, Yadong, Meng Yan, and Yi Bao. "Measurement of cable forces for automated monitoring of engineering structures using fiber optic sensors: A review." Automation in Construction 126 (2021): 103687.

[18] Ashry, Islam, et al. "A review of distributed fiber–optic sensing in the oil and gas industry." Journal of Lightwave Technology 40.5 (2022): 1407-1431.

[19] Tosi, Daniele, et al. "Fiber optic sensors for biomedical applications." Opto-mechanical fiber optic sensors. Butterworth-Heinemann, 2018. 301-333.

[20] Shanafield, M., et al. "Fiber-optic sensing for environmental applications: Where we have come from and what is possible." Water Resources Research 54.11 (2018): 8552-8557.

[21] Roman, Muhammad, et al. "Distributed fiber-optic sensing with low bending loss based on thin-core fiber." IEEE Sensors Journal 21.6 (2021): 7672-7680.

[22] Aref, S. H., M. I. Zibaii, and H. Latifi. "An improved fiber optic pressure and temperature sensor for downhole application." Measurement Science and Technology 20.3 (2009): 034009.

[23] Murphy, Kent A., and Stephen H. Poland. "Fiber optic strain and pressure sensors." Smart Structures and Materials 1997: Industrial and Commercial Applications of Smart Structures Technologies. Vol. 3044. SPIE, 1997.

[24] Yang, Y. C., and K. S. Han. "Damage monitoring and impact detection using optical fiber vibration sensors." Smart materials and structures 11.3 (2002): 337.

[25] Rao, Yun-Jiang. "Recent advances in fiber-optic FP interferometric sensors." Fundamental Problems of Optoelectronics and Microelectronics III 6595 (2007): 870-877.

[26] Richards, W. Lance. Fibre optic sensors for monitoring the structural health of aerospace vehicles. Diss. University of Wales Swansea, 2006.

[27] Inaudi, Daniele. "Application of fiber optic sensors to structural monitoring." European Workshop on Smart Structures in Engineering and Technology. Vol. 4763. SPIE, 2003.

[28] Kulik, Daria, et al. "Non-invasive blood glucose estimation using two multiplexed fiber-optic fabry-perot interferometric sensors and pulse wave signal features analysis." International Youth Conference on Electronics, Telecommunications and Information Technologies: Proceedings of the YETI 2021, St. Petersburg, Russia. Springer International Publishing, 2022.

[29] Zhu, Chen, et al. "Review of Fiber Optic Displacement Sensors." IEEE Transactions on Instrumentation and Measurement 71 (2022): 1-12.

VITA

Abhishek Prakash Hungund completed his undergraduate degree in India in 2015. He started working as a Research Engineer for CSIR-NAL's Structural Health Monitoring division in India till 2017. In 2017, he joined TATA ELXSI as an Automobile Engineer ad developed simulations for sensors used in vehicle as part of the autonomous driving systems. In 2018, he joined Qualcomm as Systems Engineer and developed data acquisition systems from mobile RF product engineering. He was promoted in 2019 to Senior Systems Engineer for his achievements and entered data analytics.

He was admitted for MS in Electrical and Computer Engineering at Missouri University of Science and Technology in 2021 spring. Shortly after which he joined the Lightwave Technology Lab to pursue thesis track towards his masters. In July of 2023, Abhishek received his Master of Science in Electrical and Computer Engineering from Missouri University of Science and Technology.

His research was focused on the development of fiber optic based interferometric sensors for air gap and thickness measurements of high temperature substances, targeting continuous casting steel industries for quality improvement and process optimization.

During summer of 2022 of his MS program, Abhishek interned at Qualcomm as a RF product Engineer, where he worked in the Mobile RF PE data analytics group. He returned to Qualcomm full-time starting June 2023 as a Lead RF Engineer.